DOI:
10.1016/j.celrep.2020.108268

Document Version
Publisher's PDF, also known as Version of record

Cell Reports

Article

Molecular Fingerprint and Developmental Regulation of the Tegmental GABAergic and Glutamatergic Neurons Derived from the Anterior Hindbrain

Graphical Abstract

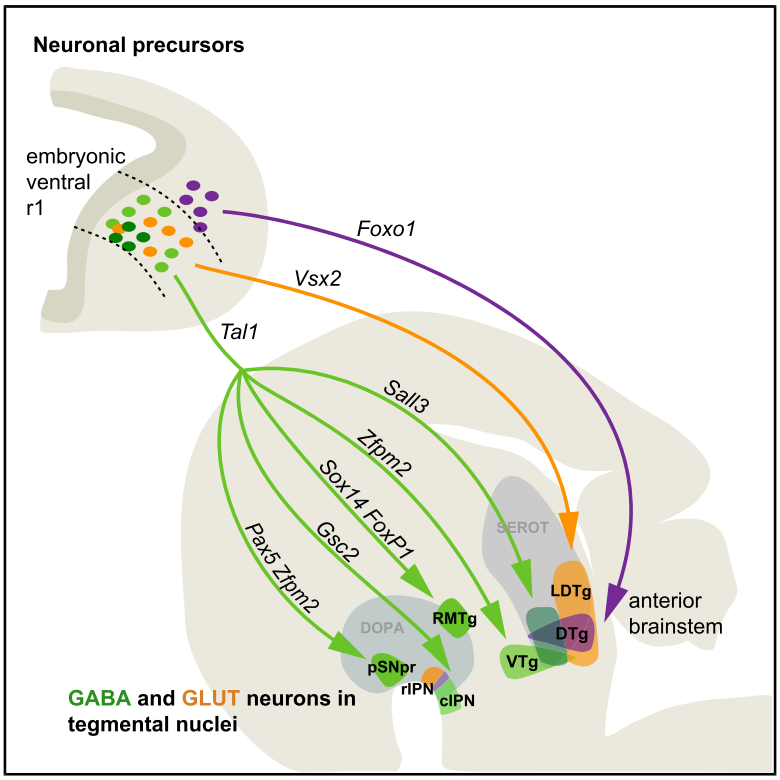

Highlights

- GABAergic and glutamatergic precursors contribute to tegmental nuclei
- The TF Tal1 and Notch signaling control neuron differentiation in the embryonic brainstem
- TFs downstream of Tal1 mark and regulate development of specific tegmental nuclei

Authors

Francesca Morello, Daniel Borshagovski, Mantas Survila, ..., Marjo Salminen, Kaia Achim, Juha Partanen

Correspondence

juha.m.partanen@helsinki.fi

In Brief

Morello et al. show how different types of neurons are generated among multipotent neuronal precursors in a specific region of the embryonic brainstem. As these neuronal precursors differentiate, they give rise to the neurons in tegmental nuclei that are highly important for the regulation of mood, motivation, movement, and memory.

Morello et al., 2020, Cell Reports *33*, 108268
October 13, 2020
https://doi.org/10.1016/j.celrep.2020.108268

CellPress

Cell Reports

CellPress
OPEN ACCESS

Article

Molecular Fingerprint and Developmental Regulation of the Tegmental GABAergic and Glutamatergic Neurons Derived from the Anterior Hindbrain

Francesca Morello,[1,6] Daniel Borshagovski,[1,6] Mantas Survila,[1,6] Laura Tikker,[1,6] Samir Sadik-Ogli,[1] Anna Kirjavainen,[1] Nuri Estartús,[1] Laura Knaapi,[1] Laura Lahti,[1] Petri Törönen,[2] Linas Mazutis,[3] Alessio Delogu,[4] Marjo Salminen,[5] Kaia Achim,[1] and Juha Partanen[1,7,*]

[1]Faculty of Biological and Environmental Sciences, P.O. Box 56, 00014 University of Helsinki, Helsinki, Finland
[2]Institute of Biotechnology, Helsinki Institute of Life Science, P.O. Box 56, 00014 University of Helsinki, Helsinki, Finland
[3]Institute of Biotechnology, University of Vilnius, 7 Sauletekio av. LT-10257, Vilnius, Lithuania
[4]Department of Basic and Clinical Neuroscience, Institute of Psychiatry, Psychology and Neuroscience, King's College London, 125 Coldharbour Lane, London SE5 9NU, UK
[5]Faculty of Veterinary Medicine, P.O. Box 66, 00014 University of Helsinki, Helsinki, Finland
[6]These authors contributed equally
[7]Lead Contact
*Correspondence: juha.m.partanen@helsinki.fi
https://doi.org/10.1016/j.celrep.2020.108268

SUMMARY

Tegmental nuclei in the ventral midbrain and anterior hindbrain control motivated behavior, mood, memory, and movement. These nuclei contain inhibitory GABAergic and excitatory glutamatergic neurons, whose molecular diversity and development remain largely unraveled. Many tegmental neurons originate in the embryonic ventral rhombomere 1 (r1), where GABAergic fate is regulated by the transcription factor (TF) Tal1. We used single-cell mRNA sequencing of the mouse ventral r1 to characterize the Tal1-dependent and independent neuronal precursors. We describe gene expression dynamics during bifurcation of the GABAergic and glutamatergic lineages and show how active Notch signaling promotes GABAergic fate selection in post-mitotic precursors. We identify GABAergic precursor subtypes that give rise to distinct tegmental nuclei and demonstrate that Sox14 and Zfpm2, two TFs downstream of Tal1, are necessary for the differentiation of specific tegmental GABAergic neurons. Our results provide a framework for understanding the development of cellular diversity in the tegmental nuclei.

INTRODUCTION

The anterior brainstem is a complex brain region that comprises anatomically and functionally distinct tegmental nuclei regulating vital processes. The tegmental nuclei contain diverse inhibitory GABAergic and excitatory glutamatergic neurons that influence both the adjacent monoaminergic neurons and other targets in the anterior brain. GABAergic neurons in the substantia nigra pars reticulata (SNpr) control voluntary movement, the GABAergic rostromedial tegmental nucleus (RMTg), and the glutamatergic laterodorsal tegmental nucleus (LDTg) regulate aversion and reward responses, whereas GABAergic and glutamatergic neurons in the ventral tegmental area (VTA) and dorsal raphe (DR) control mood and motivated behavior (Barrot et al., 2012; Brown et al., 2014; Lammel et al., 2012; Morales and Margolis, 2017; Proulx et al., 2014). In addition, GABAergic ventral and dorsal tegmental nuclei of Gudden (VTg and DTg, respectively) have been implicated in regulation of brain theta waves, memory, and spatial navigation (Vann and Nelson, 2015). To fully comprehend the important functions of these tegmental nuclei, it is essential to characterize their constituent neurons and the mechanisms that generate their diversity.

Tegmental GABAergic and glutamatergic neuron precursors largely originate in the embryonic rhombomere 1 (r1) of the hindbrain and can undergo complex tangential migrations. Some of the ventral brainstem neurons, such as glutamatergic neurons in the reticular activating system, originate in the dorsal r1, including the rhombic lip (Aroca et al., 2006; Green and Wingate, 2014; Lorente-Cánovas et al., 2012; Machold and Fishell, 2005; Rose et al., 2009). Similarly, GABAergic neurons in the interpeduncular nucleus (IPN) and medial brainstem area undergo migrations from the dorsolateral r1 (Lorente-Cánovas et al., 2012; Waite et al., 2012). Yet, other brainstem neurons, such as GABAergic neurons of the posterior SNpr (pSNpr), VTA, and RMTg, as well as glutamatergic neurons in the LDTg and IPN, are born in a ventral r1 region (rV2), molecularly similar to the V2 domain of the spinal cord (Delile et al., 2019; Joshi et al., 2009; Lahti et al., 2016; Lorente-Cánovas et al., 2012; Peng et al., 2007). In the rV2 region, proliferative neuronal progenitors expressing the transcription factor (TF) Nkx6-1 give rise to intermingled post-mitotic precursors of both

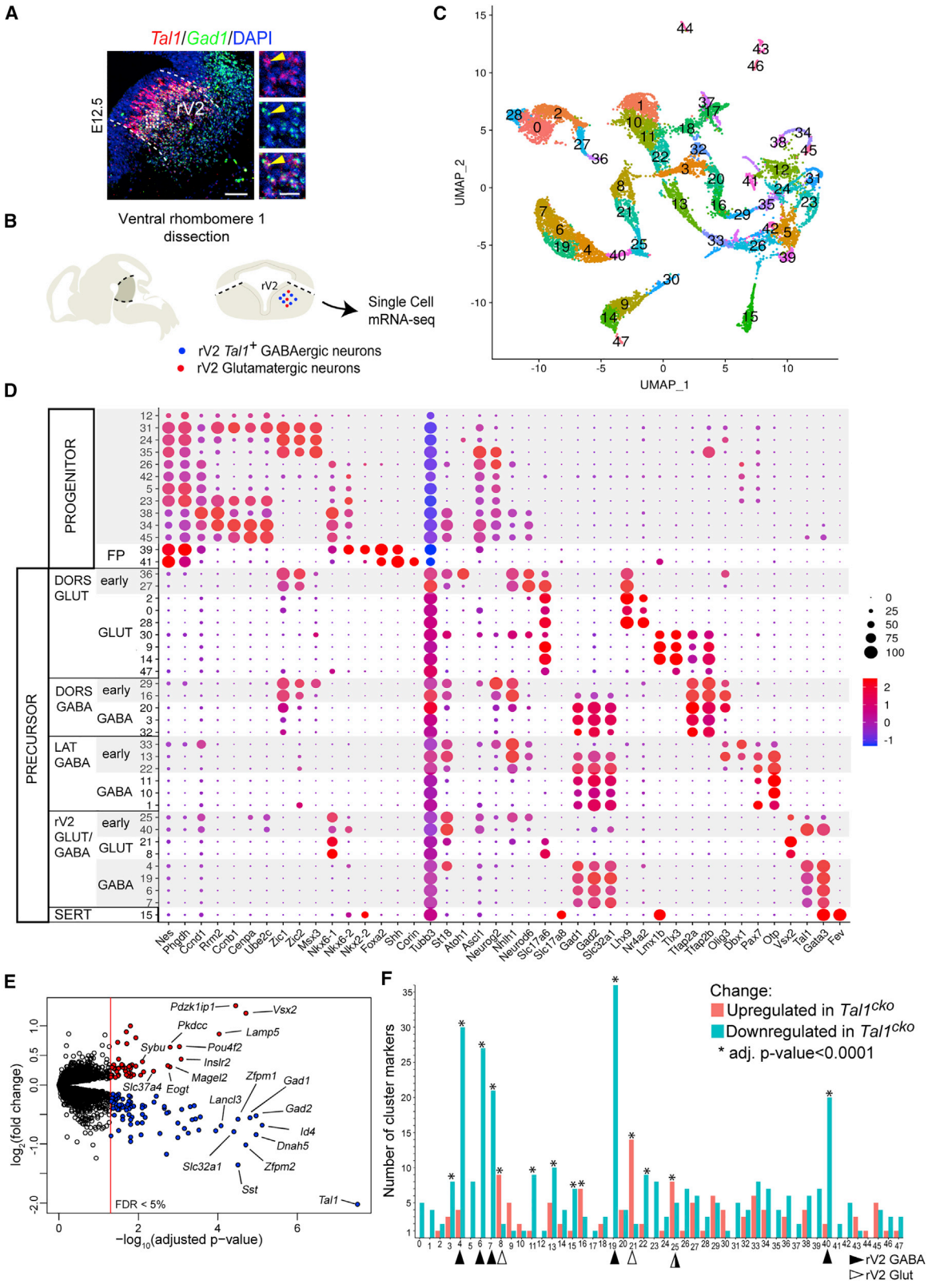

(legend on next page)

GABAergic and glutamatergic neurons (Lahti et al., 2016). In the newly born rV2 neuronal precursors, the TFs Tal1, Gata2, and Gata3 are required for differentiation into a GABAergic instead of a glutamatergic phenotype and the development of tegmental GABAergic neurons, including the pSNpr, VTA, and RMTg GABAergic neurons associated with the monoaminergic systems (Achim et al., 2012; Bradley et al., 2006; Lahti et al., 2016). Although Tal1 and Gata TFs are instrumental for GABAergic fate selection, regulatory events up- and downstream of them remain unclear. In addition to the developing brain, Tal and Gata TFs regulate gene expression in many other tissues, including hematopoietic cells, where they interact with co-factors, such as Zfpm1, to guide differentiation of distinct cell lineages (Chlon and Crispino, 2012). How the selector TFs instruct the development of tegmental neuron subtypes remains mostly unknown.

Large-scale single-cell profiling studies have revealed neuronal complexity throughout the adult mouse brain (Saunders et al., 2018; Zeisel et al., 2018). As this diversity is established during development, we used single-cell mRNA sequencing to study the differentiating neuronal populations in the embryonic mouse ventral r1. We focused on the stages of early neurogenesis, prior to the extensive gliogenesis that hampers high-throughput analyses in the adult brainstem. We characterize main cellular lineages in the r1, as well as gene regulatory cascades controlled by the GABAergic neuron selector Tal1. Our results reveal a dynamic gene expression pattern along the differentiation path of the Tal1-dependent GABAergic neurons, suggest mechanisms for separation of the GABAergic and glutamatergic branches of rV2 precursors, identify GABAergic neuron subtypes, and demonstrate requirements for TFs downstream of Tal1 in development of rV2-derived GABAergic nuclei. Our work provides a basis for understanding molecular characteristics and developmental mechanisms of the GABAergic and glutamatergic neuron subtypes in the tegmental nuclei regulating central aspects of behavior.

RESULTS

Neuronal Progenitor and Precursor Cell Types in the Embryonic Ventral r1

To examine the cellular diversity in the developing mouse ventral r1, we used single-cell transcriptional profiling. As Tal1-dependent GABAergic precursors are born in the ventral r1 at embryonic day 10.5 (E10.5) to E13.5 and move to their final destinations shortly thereafter (Achim et al., 2012; Lahti et al., 2016), we profiled the cell types undergoing neurogenesis.

Cells from wild-type E12.5 and E13.5 embryonic ventral r1 were collected using the Chromium (10xGenomics) single-cell mRNA sequencing assay (Figures 1A and 1B; Table S1). In addition, we used the InDrop method (Klein et al., 2015) to analyze the cells from both *Control* (*Ctrl*) and $En1^{Cre};Tal1^{flox/flox}$ ($Tal1^{cko}$; Lahti et al., 2016) ventral r1 at E12.5 (Figure S2; Table S1) . Clustering and analysis of the collected cells revealed similar cell types in the ventral r1 at E12.5 and E13.5 (Figures 1C, 1D, S1, and S2; Tables S2, S3, S4 and S5). The analysis of wild-type E12.5 cells revealed 47 cell clusters (Figure 1C), of which 13 contained proliferative neural progenitors (including progenitors at different dorsoventral levels and stages of cell cycle) and 29 represented post-mitotic GABAergic, glutamatergic, and serotonergic neuron precursors (Figure 1D). Based on their gene expression, the post-mitotic precursors were at different stages of differentiation and potentially contributing to a wide spectrum of tegmental nuclei.

At E12.5, both male (n = 2) and female (n = 2) embryos were separately analyzed with the Chromium assay. All of the samples revealed similar cell clusters. Other than transcripts involved in X inactivation or derived from Y chromosome genes, we found only a few quantitative differences in gene expression between the sexes (Table S5).

Identification of Tal1-Dependent Precursor Subtypes

To pinpoint the Tal1-dependent cell groups in our single-cell data, we identified the cell clusters expressing *Tal1* and its putative partners *Gata2* and *Gata3*. At E12.5, five of the GABAergic precursor clusters (clusters 40, 4, 19, 6, and 7), expressed all of these TFs (Figure 1D; Table S3). In addition, we detected some *Tal1*-, *Gata2*-, and *Gata3*-positive cells in cluster 25, which also expressed markers of early post-mitotic precursors (*St18* and *Gadd45 g*), and cluster 45, which expressed G2/M-phase, but not S-phase, markers, thus likely representing cells undergoing a terminal mitosis before post-mitotic differentiation (Figures 1D, S1B, and S1D; Table S3). We were able to assign counterparts for the E12.5 $Gata2^{+};Gata3^{+};Tal1^{+}$ GABAergic clusters in the E13.5 data (Figure S1E; Table S4). In addition to these GABAergic precursor clusters, serotonergic precursors (cluster 15) expressed *Gata2* and *Gata3*, but not *Tal1* (Figures 1D and

Figure 1. Single-Cell mRNA Sequencing of the E12.5 Mouse Ventral r1

(A) Expression of *Tal1* and *Gad1* (ISH) in the ventral r1 at E12.5. The rV2 region is indicated. Scale bars represent 50 μm (main panel) and 10 μm (close-ups).

(B) The region of the ventral r1 dissected for single-cell mRNA sequencing.

(C) Uniform manifold approximation and projection (UMAP) plot showing the clusters of ventral r1 cells from E12.5 embryos (15,027 cells from four embryos). Six of the clusters (17, 18, 37, 43, 44, and 46) represent non-neural cell types, such as hematopoietic cells, endothelial cells, and microglia. The remaining 41 clusters represent neural cell types.

(D) Dotplot of key marker expression across clusters of proliferative progenitors and of post-mitotic precursors. Dot size corresponds to the proportion of cells within a cluster expressing the gene, and the color indicates the mean expression of the gene within a cluster.

(E) Bulk mRNA sequencing of E12.5 *Ctrl* (n = 6) and $Tal1^{cko}$ (n = 6) ventral r1 tissue revealing genes down- (blue dots) and upregulated (red dots) in the $Tal1^{cko}$ tissue (adjusted $p < 0.05$).

(F) Enrichment of Tal1-dependent genes in clusters identified in the ventral r1 by single-cell mRNA sequencing. The x axis represents the clusters in the E12.5 single-cell mRNA sequencing data. The y axis shows the number of cluster markers found among differentially expressed genes in the bulk mRNA sequencing. Clusters with markers enriched for Tal1-dependent genes are marked with asterisks (*adjusted $p < 0.001$, two-tailed Fisher's exact test). The rV2 clusters are indicated with open (glutamatergic) and filled (GABAergic) triangles. Cluster 25 represents early precursors of the both lineages.

See also Figures S1 and S2 and Table S1, S2, S3, S4, S5, and S6.

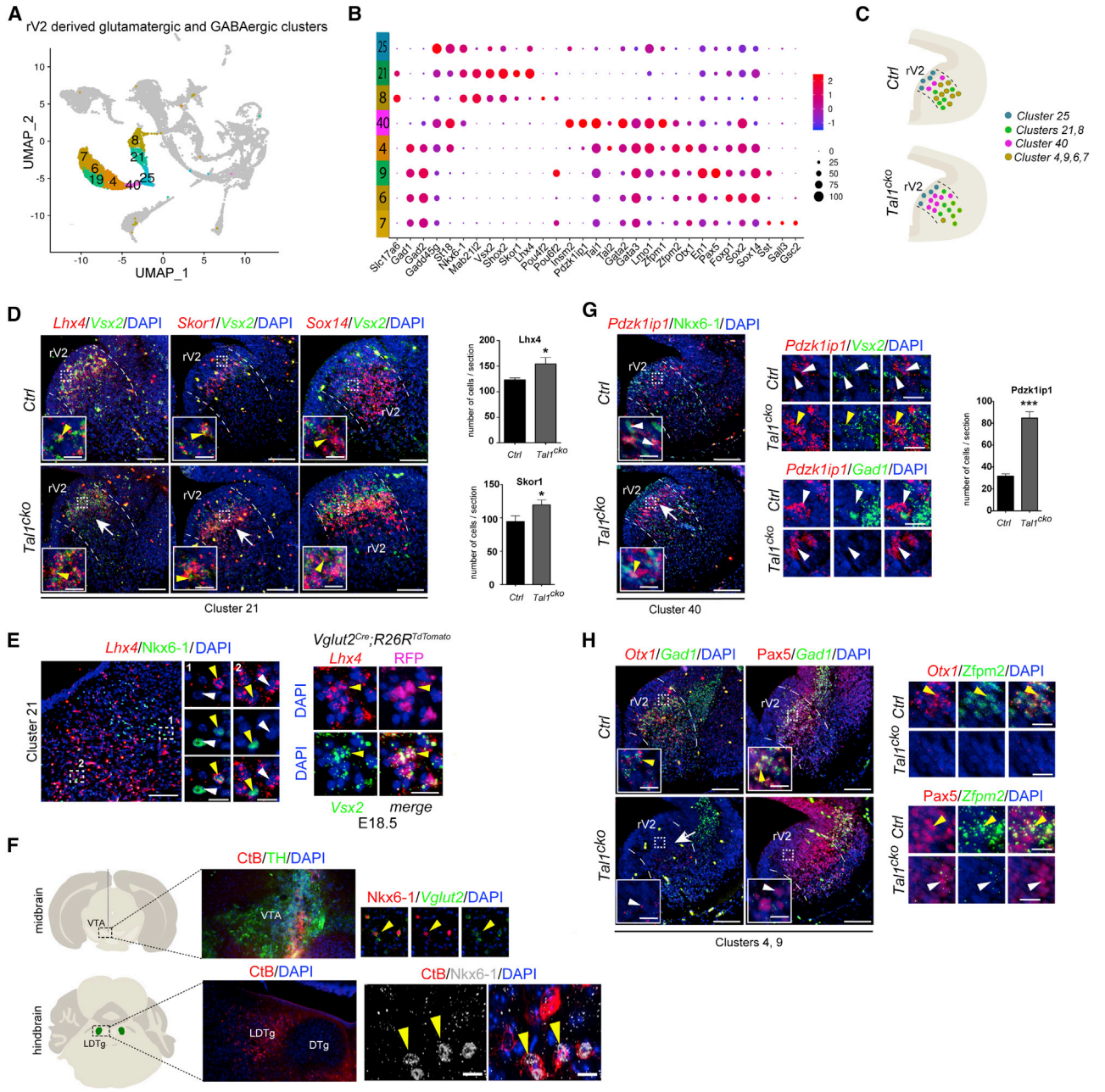

Figure 2. Characterization of rV2-Derived Glutamatergic and GABAergic Precursors

(A) UMAP plot of E12.5 ventral r1 cell transcriptomes with the rV2-derived precursor clusters highlighted.

(B) Dot plot showing the expression of selected markers of E12.5 rV2 precursor clusters.

(C) Schematic summary of the distribution of rV2 cell clusters on a coronal view of E12.5 *Ctrl* and *Tal1*^{cko} embryos.

(D) Expression of *Lhx4*, *Vsx2*, *Skor1*, and *Sox14* (ISH) in E12.5 *Ctrl* and *Tal1*^{cko} embryos. The rV2 domain is indicated by dashed lines. White arrows indicate higher levels of gene expression in *Tal1*^{cko} embryos. In close-ups of boxed areas, yellow arrowheads indicate double-positive cells. Quantification of the number of *Lhx4*- and *Skor1*-positive cells in *Ctrl* and *Tal1*^{cko} embryos is shown. Data are represented as mean ± SEM; *p < 0.05.

(E) Expression of *Lhx4* (ISH) and Nkx6-1 (IHC) in the LDTg area of E18.5 *Ctrl* embryos. In close-ups of the boxed area, white arrowheads indicate single-positive cells, yellow arrowheads double positive cells. (Right) Expression of RFP (IHC) together with *Lhx4* and *Vsx2* (ISH) in the LDTg of E18.5 *Vglut2*^{Cre}*;R26R*^{TdTomato} mice.

(F) Retrograde tracing of projections from Nkx6-1^{+} LDTg cells to the VTA. (Top) Analysis of the Choleratoxin B subunit (CtB) injection site in the adult VTA by IHC for CtB and TH. (Bottom) Analysis of the retrogradely traced cells in the LDTg by IHC for CtB. High-magnification images show the co-localization of Nkx6-1 expression with *Vglut2* (ISH) and CtB (IHC) in LDTg cells. Yellow arrowheads indicate double-positive cells.

(legend continued on next page)

S1B; Table S3), consistent with their roles in serotonergic neurogenesis (Haugas et al., 2016).

InDrop analysis of E12.5 *Ctrl* and *Tal1*^{cko} cells revealed that the *Gata2*$^{+}$;*Gata3*$^{+}$;*Tal1*$^{+}$ GABAergic cluster was mostly composed of *Ctrl* cells, suggesting that these cells are Tal1 dependent (E12.5 InDrop cluster 3, molecularly similar to E12.5 clusters 40, 4, 19, 6, and 7 and E13.5 clusters 4, 5, and 28; Figure S2; Tables S2, S3, and S4). Finally, we compared gene expression in the ventral r1 tissue between E12.5 *Ctrl* and *Tal1*^{cko} embryos using bulk mRNA sequencing and identified genes whose expression was altered in the *Tal1*^{cko} tissue (Figure 1E; Table S6). The genes expressed in the E12.5 *Gata2*$^{+}$;*Gata3*$^{+}$;*Tal1*$^{+}$ GABAergic precursors (clusters 40, 4, 19, 6, and 7) were highly overrepresented among genes downregulated in the *Tal1*^{cko} mutants (Figure 1F). We found genes upregulated in the *Tal1*^{cko} embryos among the ones expressed in the early GABAergic/glutamatergic precursors (cluster 25) and glutamatergic precursors of the rV2 (clusters 21 and 8, see below) (Lahti et al., 2016).

In summary, single-cell analyses identified several groups of Tal1-dependent GABAergic precursors in the ventral r1, possibly representing different developmental stages and GABAergic neuron subtypes.

Anatomical Characterization of the Precursor Subtypes in the Ventral r1

To validate the single-cell mRNA sequencing results and to understand the anatomical localization of the precursor cell types, we characterized the expression of their marker genes in the embryonic ventral r1. We analyzed the tissue distribution of both Tal1-dependent (rV2) and Tal1-independent (dorsal and lateral) precursor cell types.

Dorsally Derived Glutamatergic and GABAergic Precursors

Several types of neurons originate in the embryonic dorsal r1 and migrate tangentially to its ventral part. These include glutamatergic precursors that express *Lhx9* or *Lmx1b* and populate several nuclei in the brainstem (Green and Wingate, 2014; Millen et al., 2014; Rose et al., 2009). Consistently, we identified precursor subtypes expressing *Lhx9* (clusters 36, 27, 2, 0, and 28) or *Lmx1b*/*Tlx3* (clusters 30, 9, 14, and 47) (Figure 1D, Figures S3A and S3B; Tables S2 and S3). Using fluorescence *in situ* hybridization (ISH) and immunohistochemistry (IHC), we showed that *Lhx9*- and *Lmx1b*-expressing precursors locate in distinct domains of the lateral r1 at E12.5 (Figures S3C and S3D).

In addition to glutamatergic precursors, some GABAergic subtypes (clusters 35, 29, 16, 20, 3, and 32) also expressed dorsal markers, such as *Zic1* and *Skor1* (Figures 1D, S3E, and S3F; Tables S2 and S3) (Nagai et al., 1997). Both dorsal glutamatergic *Lhx9*$^{+}$ and *Lmx1b*$^{+}$ cells, as well as dorsal GABAergic *Skor1*$^{+}$ cells, included clusters enriched for immature precursor markers, such as *Gadd45 g*, *Nhlh1, Cntn2*, and *Insm1* (Figures S3B and S3F; Tables S2 and S3), suggesting that they represent precursors at earlier stages of differentiation (Ratié et al., 2014; Tavano et al., 2018). Using ISH, we detected *Skor1*$^{+}$;*Gad1*$^{+}$ cells in the dorsocaudal part of the E12.5 r1, where they likely represented post-mitotic precursors derived from *Zic1*$^{+}$;*Pax3*$^{+}$ progenitors in the adjacent ventricular zone (Figures S3G and S3H). These glutamatergic and GABAergic precursors may contribute to subtypes of excitatory and inhibitory neurons in the anterior brainstem.

Laterally Derived GABAergic Precursors

Six of the E12.5 GABAergic clusters expressed *Otp*, suggesting an origin in the lateral r1 (Figures 1D, S3E, and S3F) (Lorente-Cánovas et al., 2012). We found the *Otp*$^{+}$ cells divided into anatomically different cell groups expressing *Cntn2*, *Foxo1*, or *Ntn1* (Figures S3G and S3H). Again, the *Cntn2*$^{+}$ cells appeared to represent immature precursors, possibly giving rise to the *Foxo1*$^{+}$ and *Ntn1*$^{+}$ precursors. All of these *Otp*$^{+}$ cell populations expressed different levels of *Pax7*, a marker for alar-plate-derived neurons. In addition to the IPN (Lorente-Cánovas et al., 2012), we showed that the *Foxo1*$^{+}$ cells contribute to the DTg (Figure 6, see below). In turn, we found that *Ntn1*$^{+}$ cells also expressed *Pitx2*, a marker of Tal1-independent GABAergic neurons in the medial r1 (Figure S3H) (Lahti et al., 2016; Waite et al., 2012).

Both the glutamatergic and GABAergic subtypes migrating tangentially toward the floor plate expressed Robo receptors in a complementary pattern; *Robo3* was expressed in the putative early precursors and *Robo2* in the more mature precursors (Figure S3F; Table S3). The Robo receptors may thus coordinate the tangential migration of the anterior brainstem precursors similar to the precerebellar neurons derived later from the more caudal hindbrain (Marillat et al., 2004).

rV2-Derived Glutamatergic and GABAergic Precursors

In addition to the GABAergic marker *Tal1* and the glutamatergic marker *Vsx2*, we detected a number of gene products enriched in the rV2-derived cell populations (Figures 1D, 2A, and 2B; Tables S3). One of the *Vsx2*$^{+}$ glutamatergic clusters (cluster 21) expressed the TFs *Lhx4*, *Skor1*, *Shox2*, and *Sox14.* In E12.5 *Ctrl* brain, we detected *Lhx4*, *Skor1*, and *Shox2* expression in *Vsx2*$^{+}$ post-mitotic precursors in the rV2 mantle zone (Figures 2C, 2D, and S4E). In the rV2 of *Tal1*^{cko} brain, the number of both *Lhx4*- and *Skor1*-expressing cells was increased (*Ctrl* versus *Tal1*^{cko}, $p < 0.05$; Figure 2D), likely reflecting a fate change in mutant precursors (Lahti et al., 2016). We also observed

(G) Expression of *Pdzk1ip1* (ISH) and Nkx6-1 (IHC). The white arrow indicates higher level of expression of *Pdzk1ip1* in *Tal1*^{cko} mice. In close-ups of the boxed areas, white arrowheads indicate single-positive cells, and yellow arrowheads indicate co-expression in *Tal1*^{cko} mice. (Right) Close-up images showing the expression of *Pdzk1ip1* with the rV2 glutamatergic marker *Vsx2* and GABAergic marker *Gad1* in *Ctrl* and *Tal1*^{cko} embryos. Quantification of *Pdzk1ip1*$^{+}$ cells in *Ctrl* and *Tal1*^{cko} embryos is shown. Data are represented as mean ± SEM; ***$p < 0.001$.

(H) Expression of *Otx1*, *Gad1* (ISH), and Pax5 (IHC) in the rV2 domain. In close-ups of boxed areas, white arrowheads indicate single-positive cells, and yellow arrowheads indicate double-positive cells. (Right) Close-ups show the expression of *Otx1* (ISH) and Pax5 (IHC) with the rV2 GABAergic marker *Zfpm2* in *Ctrl* and *Tal1*^{cko} embryos. White arrowheads indicate single-positive cells, and yellow arrowheads indicate double-positive cells.

Scale bars represent 50 μm (main panels), 10 μm (close-ups in D, G, and H), 20 μm (close-ups in E), and 7 μm (close-ups in F). VTA, ventral tegmental area; LDTg, laterodorsal tegmental nucleus; DTg, dorsal tegmental nucleus of Gudden. See also Figure S4 and Tables S2 and S3.

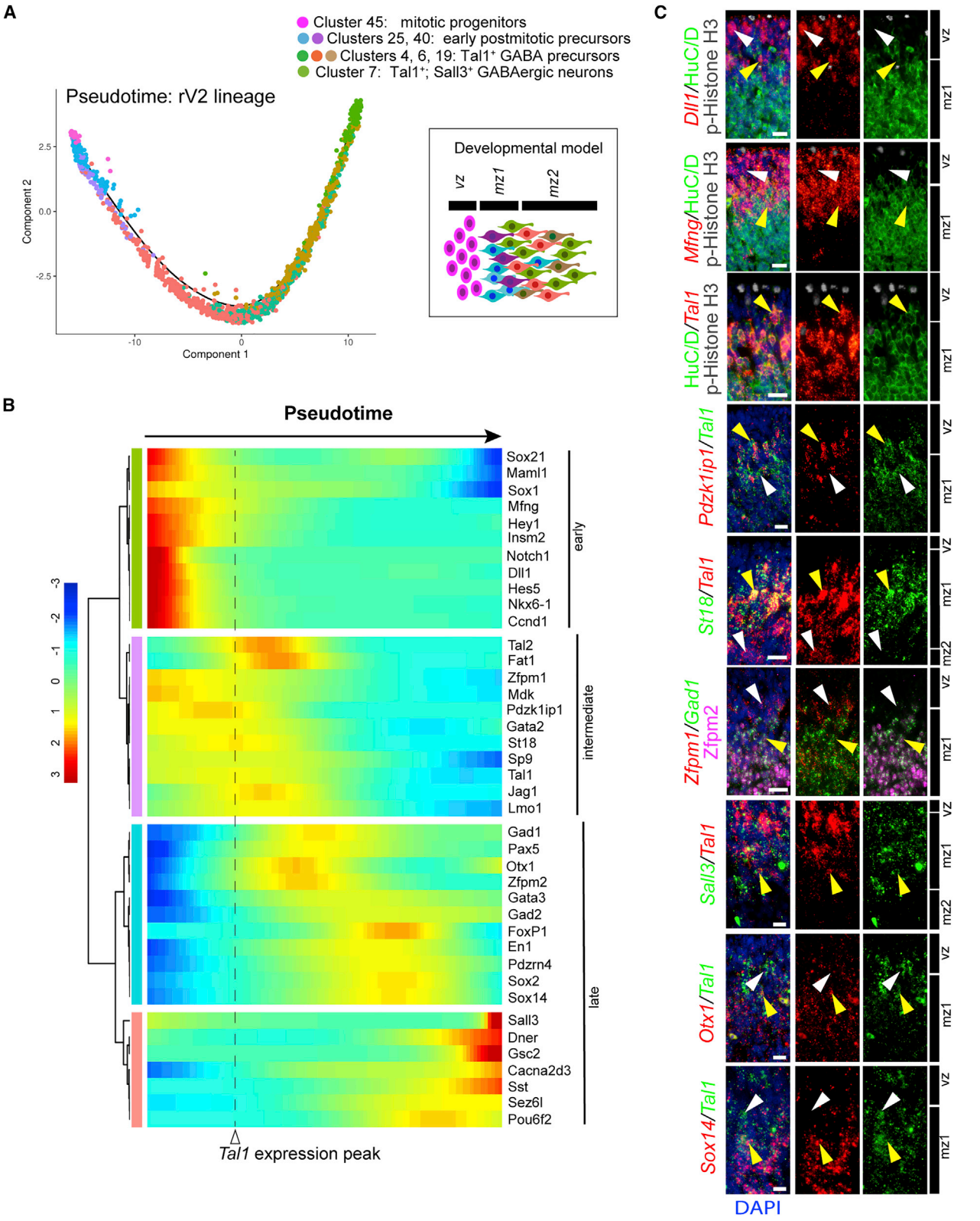

(legend on next page)

Sox14^{+};*Vsx2*$^{+}$ cells in both *Ctrl* and *Tal1*^{cko} brain, but in the *Tal1*^{cko}, most of the *Sox14*$^{+}$ cells also expressed *Vsx2* (Figure 2D). As the *Vsx2*$^{+}$ cells give rise to glutamatergic neurons in the LDTg and IPN (Lahti et al., 2016), we analyzed the expression of the identified markers in these nuclei. *Skor1* and *Shox2* expression was not detectable in the perinatal brain (data not shown). In contrast, at E18.5, we detected *Lhx4* expression specifically in glutamatergic neurons in the rostral LDTg, including Nkx6-1^{+} neurons, but not in the IPN (Figure 2E). By retrograde tracing, we showed that the Nkx6-1^{+} LDTg neurons project to the VTA (Figure 2F) and may thus contribute to the glutamatergic LDTg-VTA projection implicated in the control of reward behavior (Lammel et al., 2012).

Next, we analyzed the genes *Sox14*, *Sox21*, *Otx1*, *Pax5*, *Id4*, and *Sst*, as their expression was enriched in rV2 GABAergic precursors (clusters 40, 4, 19, 6, and 7), (Figures 1D, 2A, and 2B; Table S3). In addition to glutamatergic precursors, we found expression of two related TFs, *Sox14* and *Sox21*, in both overlapping and specific subsets of embryonic rV2 GABAergic precursors, and they later marked distinct subtypes of tegmental neurons, including the RMTg, SNpr, and Retrorubral field (RRF) (Figure 2B, 2D, and S4A–S4D). The expression of *Sox21* was unaltered in *Sox14*$^{gfp/gfp}$ mutant embryos (Delogu et al., 2012) (Figures S4C and S4D; data not shown), suggesting independent regulation of these two TFs. *Otx1* and Pax5 were co-expressed with *Gad1* and Zfpm2 in the GABAergic rV2 mantle precursors of *Ctrl* embryos (Figure 2H). In *Tal1*^{cko} mutants, *Otx1*, *Id4*, and *Sst* expression was lost in the rV2 precursors (Figures 2H and S4E).

Some of the rV2 cell clusters represented precursors at various stages of post-mitotic differentiation. We found that the rV2-derived glutamatergic and GABAergic precursor clusters were connected by a cell cluster negative for the expression of definitive glutamatergic or GABAergic markers (cluster 25). These cells expressed *Gadd45 g*, *St18*, and *Btg2/Tis21*, characteristic of early neuronal precursors (Figure 2B; Table S3) (Canzoniere et al., 2004; Matsushita et al., 2014; Ratié et al., 2014). They also contained some cells positive for TFs typical for glutamatergic (*Nkx6-1* and *Vsx2*) and GABAergic (*Tal1* and *Gata2*) lineages. In the early GABAergic cells next to the bifurcation of the rV2 GABAergic and glutamatergic lineages (cluster 40), the expression of a putative Notch regulator *Pdzk1ip1* was highly enriched (Figure 2B; Tables S3) (Garcia-Heredia et al., 2017). In E12.5 *Ctrl* embryos, *Pdzk1ip1*$^{+}$ cells were located in the rV2 mantle zone, close to the ventricular zone (Figure 2G). Their number was significantly increased in *Tal1*^{cko} embryos (*Ctrl* versus *Tal1*^{cko}, $p < 0.001$), consistent with our bulk mRNA sequencing demonstrating *Pdzk1ip1* upregulation in the ventral r1 of *Tal1*^{cko} embryos (Figure 2G; Table S6). In *Ctrl* embryos, *Pdzk1ip1* transcripts co-localized with *Tal1*, but not with *Gad1*, *Nkx6-1*, or *Vsx2* (Figures 2G and 3C). In *Tal1*^{cko} embryos, we found *Pdzk1ip1* and *Vsx2* expression in the same cells, suggesting that the loss of *Tal1* affects GABAergic fate in early *Pdzk1ip1*$^{+}$ precursors.

In summary, we located the precursor cell clusters revealed by single-cell mRNA sequencing in embryonic r1 tissue. In rV2 precursors, we revealed both shared and unique gene expression features in glutamatergic and GABAergic precursors. In addition to precursors of different neuronal subtypes, we observed unique gene expression in precursors at different stages of post-mitotic development. These include early precursors of both rV2 GABAergic and glutamatergic neurons and GABAergic precursors after bifurcation of the rV2 GABAergic and glutamatergic lineages.

The Differentiation Path of Tal1-Dependent GABAergic Precursors

To further reveal gene expression changes during the course of the rV2 GABAergic neuron differentiation, we pseudotemporally ordered the E12.5 rV2 mitotic cells (cluster 45), early post-mitotic precursors (cluster 25), and maturing Tal1-dependent precursors (clusters 40, 4, 19, 6, and 7). The general order of the clusters on the inferred trajectory was consistent with cell lineage progression. The lineages start with mitotic cells, followed by early and maturing post-mitotic precursors (Figure 3A). Over the pseudotime, we found statistically significant changes in the expression of 5,856 genes, including Notch pathway components and several TFs expressed in the rV2 GABAergic neuron clusters (Table S7).

To understand the gene co-expression dynamics during the cell lineage progression, we visualized the expression of pseudotime-dependent Notch pathway members and TFs marking the subclusters of *Tal1*$^{+}$ precursors over the inferred differentiation trajectory (Figure 3B). Tissue expression of representative members of early, intermediate, and late genes was consistent with their expression order over the pseudotime sequence (Figure 3C, and data not shown). We detected the expression of several Notch pathway genes, including *Dll1* and *Mfng*, in ventricular zone progenitors and early post-mitotic precursors (Figures 3B and 3C). *Tal1* and several of its co-regulators, such as *Gata2*, *Tal2*, *Zfpm1*, and *Lmo1*, were in the intermediate group (Figure 3B). The intermediate group also contained the TFs *St18* and *Insm2* as well as *Pdzk1ip1*. The dynamics of their expression in E12.5 ventral r1 tissue matched the expression of these genes specifically in the early precursor clusters (clusters 25 and 40) (Figures 3C and 2B; Table S3).

Figure 3. Differentiation Path of the Tal1-Dependent rV2 GABAergic Precursors

(A) Pseudotime ordering of E12.5 cells of the rV2 GABAergic lineage. (Right) Schematic illustration of Tal1-dependent precursor differentiation, from ventricular zone mitotic cells to mantle zone 1 (mz1) immature precursors and further differentiated precursors in the more basal mantle zone 2 (mz2).

(B) Heatmap of the expression levels of selected marker genes across pseudotime-ordered cells of the rV2 GABAergic lineage. The peak of *Tal1* expression is indicated by a dashed line.

(C) Expression of early (*Dll1* and *Mfng*), intermediate (*Pdzk1ip1*, *St18*, and *Zfpm1*), and late (*Zfpm2*, *Sall3*, *Otx1*, and *Sox14*) markers of GABAergic differentiation in the rV2 domain, shown together with *Tal1*, p-histone H3 (an M-phase marker), or HuC/D (a post-mitotic marker) (ISH and IHC). The border between the ventricular zone and mz1 is based on the HuC/D expression. White arrowheads show single-positive cells, and yellow arrowheads indicate double-positive cells.

Scale bar, 20 μm. See also Table S7.

We found that *Gata3* and *Zfpm2* were activated after the other Tal/Gata complex members, and their expression continued in the maturing precursors (Figures 3B and 3C). Additional genes of the late group contained Tal1-dependent TFs, such as *Otx1*, *FoxP1*, *Sox14*, and *En1*, expressed in specific subsets of GABAergic neurons (see above and Lahti et al., 2016). *Sall3*- and *Gsc2*-expressing precursors were located at the end of the pseudotime trajectory (Figures 3A and 3B). However, our analyses of *Sall3* expression at later stages of development did not support the conclusion that all the precursors end up with a *Sall3*$^{+}$ phenotype (Figure 5; see below). Rather, *Sall3*-expressing GABAergic precursors may have progressed further in their differentiation.

In summary, these results revealed sequential expression of gene products, including Notch pathway genes, Gata-Tal complex components, and Tal1-dependent TFs, during rV2 GABAergic neuron differentiation.

Bifurcation of the Glutamatergic and GABAergic rV2 Precursor Lineages

Our results suggested that the rV2 glutamatergic and GABAergic neurons share a pool of common precursors. Using pseudotemporal ordering of both E12.5 and E13.5 rV2 precursors, we addressed the bifurcation of these lineages. The analysis of the E13.5 precursors is described below. The E12.5 dataset gave highly similar results (data not shown). Of the E13.5 precursors, we included cells in cluster 36 (similar to E12.5 cluster 25), which represented common precursors exiting the cell cycle; post-mitotic GABAergic clusters 28, 5, 4, and 9 (similar to E12.5 clusters 40, 4, 19, 6, and 7), and post-mitotic glutamatergic clusters 18 and 12 (similar to E12.5 clusters 21 and 8) (Figures S1C and S1E). Pseudotemporal ordering of these cells revealed a lineage tree with a branch point between glutamatergic and GABAergic lineages (Figures 4A, 4D, and 4E). Analysis of gene expression dependent on this branch point revealed 23 modules of genes sharing similar patterns of expression (Table S8). These included gene products involved in mitotic division and cell-cycle exit found in very early precursors (gene modules 12, 16, 13, 14, and 22) and gene products involved in later neuronal maturation (gene modules 4, 9, and 19; Figures 4B and 4C; Table S8). Notably, we identified gene modules with biased expression in either the glutamatergic or GABAergic lineages. In particular, gene module 21 marked early GABAergic precursors and modules 1 and 8 marked more mature GABAergic precursors, whereas gene modules 7 and 11 marked the early and more mature glutamatergic precursors, respectively (Figures 4D–4I, Table S8). Genes in the early GABAergic module 21 contained several targets of Notch signaling and were highly enriched for *Hes* and *Hey* family genes; out of a total of 11 *Hes*/*Hey* gene family members, 4 genes (*Hes5*, *Hey1*, *Hey2*, and *Heyl*) were expressed in gene module 21 (hypergeometric $p < 8.04e\text{-}07$; Figure 4K). In turn, the early glutamatergic module 7 contained the Notch ligand genes *Dll4* and *Dll3*, as well as *Hes6*, suggested to negatively regulate *Hes5* function (Fior and Henrique, 2005) (Figure 4J). Gene Ontology analysis of biological pathways further revealed a significant enrichment of the term "Notch signaling pathway" both in gene module 21 (adjusted $p = 0.0062$) and in module 7 (adjusted $p = 0.019$) (Table S8).

In addition to the canonical Notch pathway genes, the early GABAergic gene module 21 included *Pdzk1ip1*, *Ttyh1*, *Cbfa2t3*, and *Angpt1*, whereas the early glutamatergic module 7 included *Mybl1*, *Nhlh1*, *Cbfa2t2*, and *Sstr2*. These genes are potentially involved in the regulation of Notch signaling, gene expression, and intercellular communication during lineage bifurcation (Figures 4J, 4K, and 4N).

Notch Signaling in Glutamatergic and GABAergic rV2 Precursor Fate Selection

As the pseudotime analysis suggested that Notch signaling is involved in GABAergic and glutamatergic lineage separation, we characterized Notch signaling activity in the GABAergic precursors by IHC for the cleaved Notch1 intracellular domain (NICD). We detected NICD in the Gata3^{+} early precursors near the ventricular zone, but not in the more mature precursors positive for Gata3 and *Gad1* expression (Figure 4L). This is consistent with the order of expression of *Hes5*, *Gata3*, and *Gad1* along the pseudotime sequence (Figure 4K and 3B; data not shown).

To test the requirement of Notch signaling for GABAergic precursor differentiation in the ventral r1, we analyzed the expression of the GABAergic neuron markers *Gad1*, *Tal1*, and Gata3 in the rV2 region in the *Presenilin 1* (*Psen1*) mutant mouse strain (De Strooper et al., 1998). In E12.5 *Psen1*$^{-/-}$ mutant embryos, where Notch signaling is defective, the expression of *Tal1*, Gata3, and *Gad1* was markedly reduced in the ventral r1 (Figure 4M). In contrast to the rV2 region, *Gad1* was still detected in the more dorsal and lateral r1. The loss of *Gad1*, *Tal1*, and Gata3 expression was concomitant with the overexpression of Vsx2 in the rV2 domain, suggesting that glutamatergic neurons may be produced at the expense of GABAergic neurons. Although some *Tal1* expression was still maintained, the phenotype of *Psen1*$^{-/-}$ embryos highly resembles the *Tal1*^{cko} phenotype (Figure 4M) (Lahti et al., 2016). In conclusion, the analysis of *Psen1* mutant mice suggests that Notch signaling is involved in the cell fate determination in the ventral r1, where cleavage of the Notch receptor might be specifically required in rV2 neuronal precursors to commit to the GABAergic fate (Figure 4N).

Development of Tal1-Dependent Sall3^{+} Precursors into GABAergic Neurons Adjacent to the DR

One of the rV2 GABAergic precursor clusters (E12.5 cluster 7; Figures 2B and 5A) expressed the TF genes *Gsc2* and *Sall3*. Although *Gsc2* and *Sall3* expression patterns partly overlapped (Figure 5A), *Gsc2*$^{+}$ and *Sall3*$^{+}$ precursors appeared to differentiate into distinct GABAergic neuron subtypes. Whereas *Gsc2*-expressing precursors gave rise to IPN neurons (Funato et al., 2010; Ruiz-Reig et al., 2019) (data not shown), *Sall3* marked a distinct type of *Tal1*$^{+}$ GABAergic cells. Analysis of the glutamatergic and GABAergic lineage branch point identified a GABAergic precursor gene module (module 8) containing *Sall3* (Table S8), suggesting that the *Sall3*$^{+}$ precursors segregate from the other GABAergic rV2 precursors early in their differentiation. In E12.5 *Ctrl* embryos, we found *Sall3* expression in GABAergic precursors in the rV2 close to the ventricular zone, particularly in its medial (ventral) half (Figure 5B). In *Tal1*^{cko} embryos, the expression of *Sall3* was specifically lost in the rV2, while ventricular zone progenitors and other ventral r1

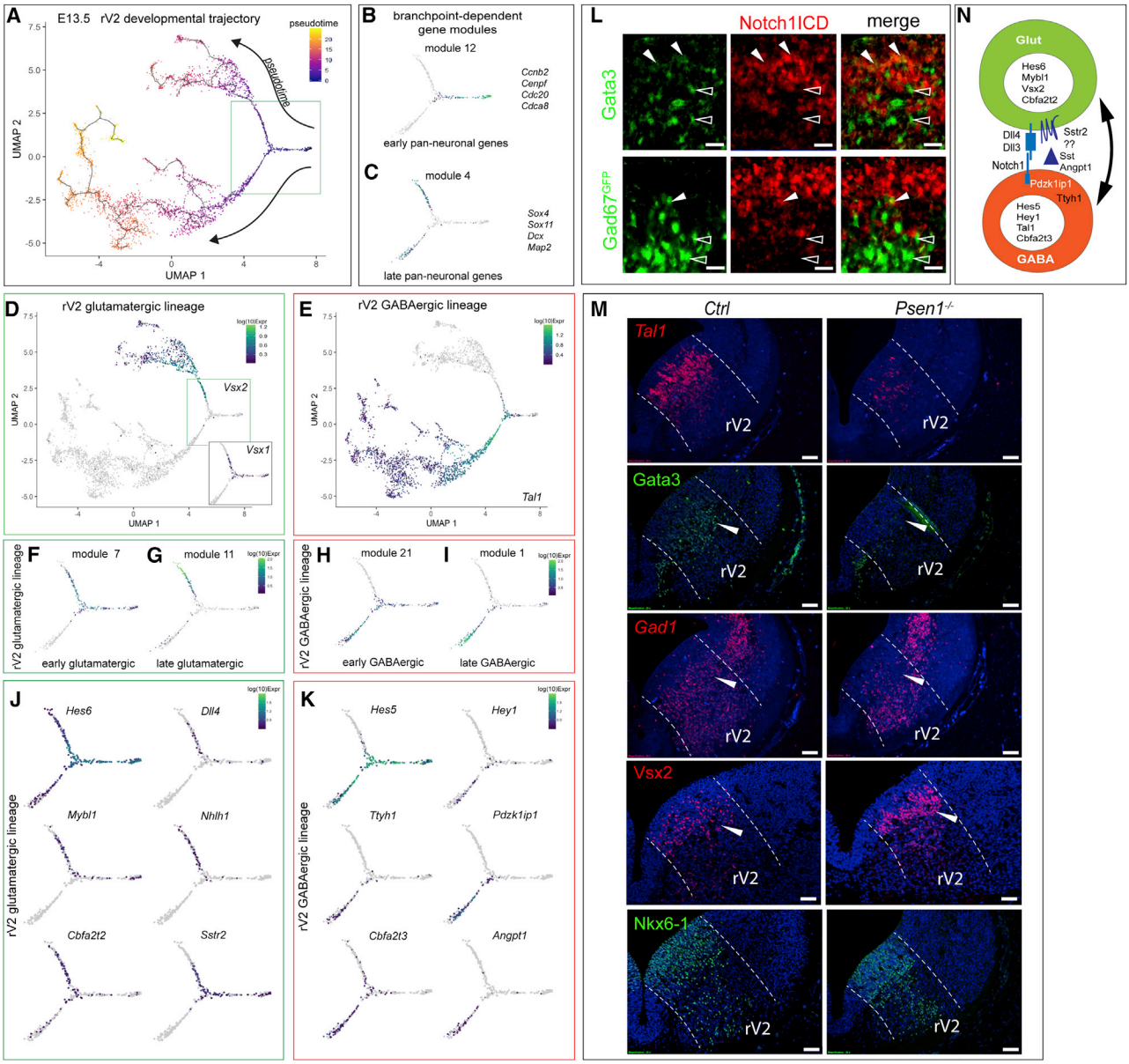

Figure 4. Branching of the rV2-Derived Glutamatergic and GABAergic Lineages

(A) UMAP plot of E13.5 rV2 GABAergic and glutamatergic cells and direction of the pseudotime trajectory. Clusters included were 36 (common precursors); 28, 5, 4, and 9 (GABAergic clusters); and 18 and 12 (glutamatergic clusters). Although *Tal1*$^{+}$, the cluster 29 was excluded, as comparison with precursor transcriptomes from the embryonic midbrain suggested that it represents a midbrain contamination (our unpublished results). The branch point of the GABA- and glutamatergic cell lineages (branch point 25) is indicated with a square.

(B–K) Genes showing similar expression dynamics along the pseudotime trajectory (gene modules) at branchpoint 25. (B) Module 12 contains genes characteristic of early neuronal precursors at terminal mitosis (*Ccnb2*, *Cenpf*, *Cdc20*, and *Cdca8*). (C) Module 4 contains genes characteristic of maturing neuronal precursors (*Sox4*, *Sox11*, *Dcx*, and *Map2*). (D) Expression of *Vsx2* over the pseudotime trajectory. Inset shows the expression of *Vsx1* in the precursors prior to the emergence of *Vsx2*-expressing cells. (E) Expression of *Tal1* over the pseudotime trajectory. (F–I) Gene modules showing asymmetric expression at the branchpoint and associated with early and late GABAergic or glutamatergic precursors. (J) Expression of genes belonging to glutamatergic gene module 7 or 11. (K) Expression of genes belonging to GABAergic gene module 21 or 1. Both glutamatergic and GABAergic modules contain a number of genes belonging to the Notch signaling pathway.

(L) Co-IHC of Notch1 intracellular domain (NICD) with Gata3 or GFP in the rV2 of E12.5 *Gad67*^{EGFP} embryos.

(M) *Tal1*, Gata3, *Gad1*, Vsx2, and Nkx6-1 expression in E12.5 *Ctrl* and *Psen1*$^{-/-}$ embryos (ISH and IHC). The Nkx6-1-positive rV2 region is delineated. Arrowheads indicate the area of downregulated *Tal1*, Gata3, and *Gad1* expression, coinciding with Vsx2 upregulation.

(N) Model of the signaling molecules, Notch pathway effectors, and TFs involved in the GABAergic versus glutamatergic lineage split.

Scale bars represent 20 μm (L) and 50 μm (M). See also Table S8.

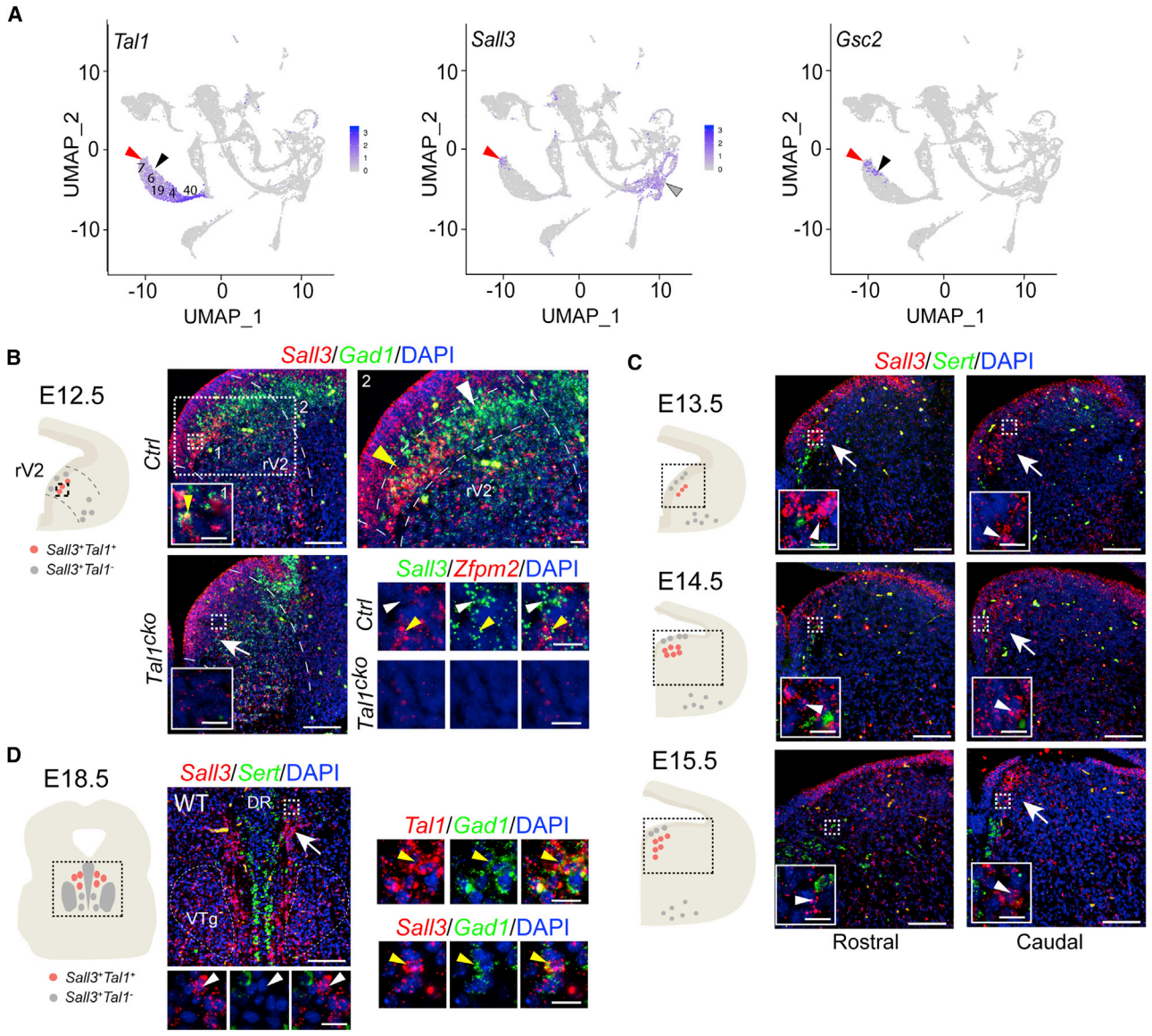

Figure 5. Tal1-Dependent *Sall3*$^+$ Precursors Give Rise to GABAergic Neurons Adjacent to the Dorsal Raphe (DR)

(A) UMAP plots showing the expression of *Tal1*, *Sall3*, and *Gsc2* in E12.5 clusters. Red arrowheads mark *Sall3* and *Tal1* co-expression in cluster 7, the gray arrowhead marks additional cells expressing *Sall3*, and black arrowheads mark cells expressing *Gsc2* but not *Sall3*.

(B) *Sall3 and Gad1* expression in the E12.5 ventral r1 (ISH). In *Ctrl* embryos, *Sall3* is expressed in the ventricular zone, medial (ventral) rV2 precursors close to the ventricular zone (indicated by the yellow arrowhead; the white arrowhead shows a *Sall3*-negative area), and a few cells in the ventral r1. In *Tal1*^{cko} embryos, *Sall3* expression is lost in medial rV2 precursors (white arrow). ISH analysis of *Sall3* and *Zfpm2* expression in the rV2 of E12.5 *Ctrl* and *Tal1*^{cko} embryos. White arrowheads indicate single-positive cells, and yellow arrowheads indicate double-positive cells.

(C) *Sall3* and *Sert* expression in the brainstem at E13.5, E14.5, and E15.5 (ISH). White arrows indicate the Tal1-dependent *Sall3* population in the rV2. In close-ups of boxed areas, white arrowheads indicate single-positive cells.

(D) *Sall3* and *Sert* expression in the E18.5 DR region (white arrow) (ISH). Close-ups show *Sall3*$^+$ cells (white arrowheads). (Right) High-magnification images of parallel sections of E18.5 brainstem showing co-expression of *Tal1* and *Gad1* (top) and *Sall3* and *Gad1* (bottom).

VTg, ventral tegmental nucleus of Gudden. Schematic illustrations show *Sall3*-expressing populations with the Tal1-dependent population highlighted (red). Scale bars represent 50 μm (main panels) and 10 μm (close-ups).

precursors maintained *Sall3* expression (Figure 5B). In *Ctrl* embryos at later stages, *Sall3* expression continued in the medial r1 (Figure 5C), increasing toward the caudal r1 and marking a region flanking the DR. At E18.5, we found *Sall3*$^+$ cells in an area delimited by the caudal part of the DR and VTg (Figure 5D). ISH on parallel sections showed that the dorsal part of this region expressed *Tal1*. Some *Sall3*$^+$ cells were also present in the VTg but were *Zfpm2* negative (data not shown; see below).

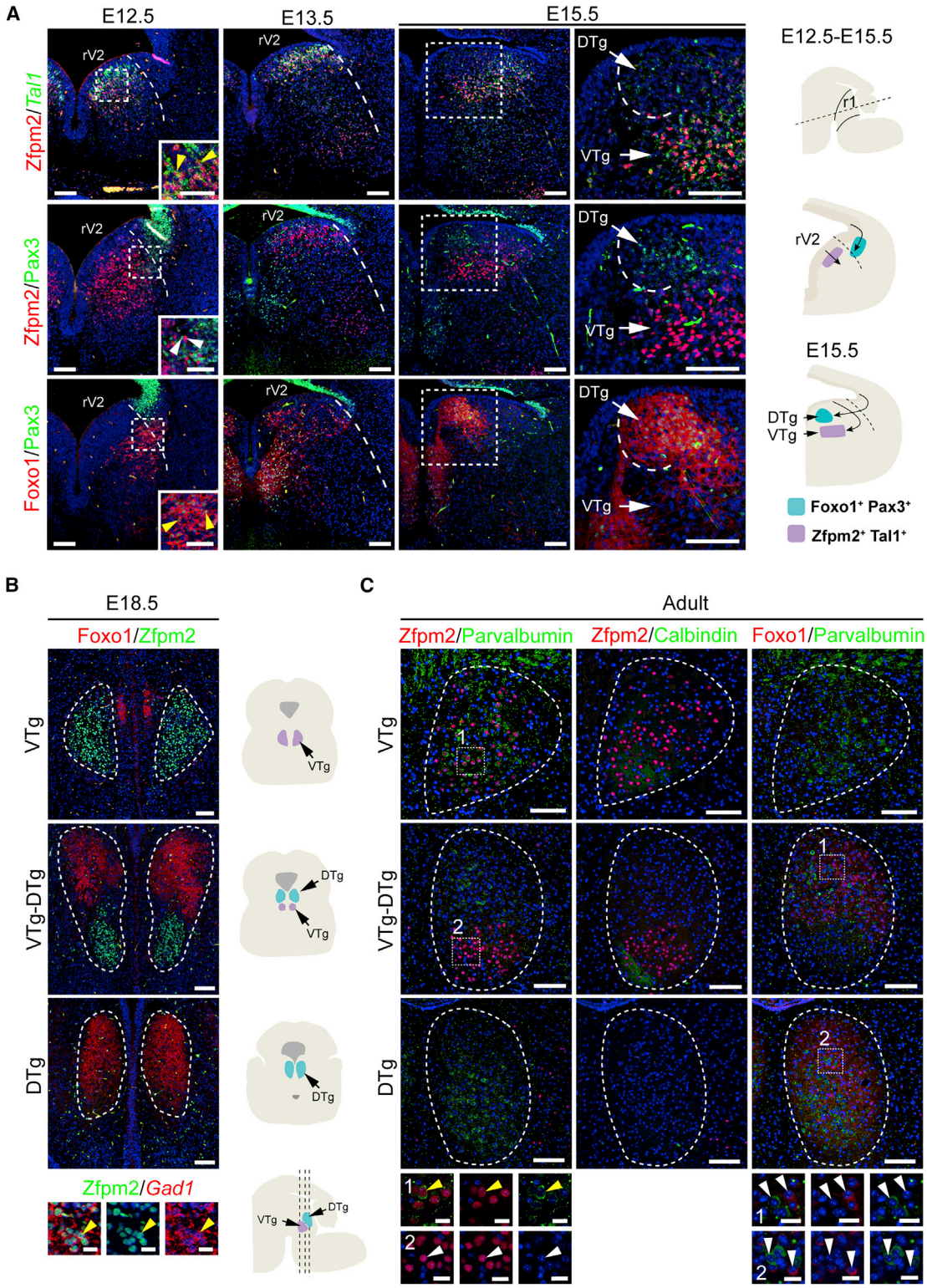

Figure 6. Zfpm2 and Foxo1 Expression in the Developing and Mature VTg and DTg

(A) Origin and development of VTg and DTg from E12.5 to E15.5. VTg precursors co-express Zfpm2 (IHC) and *Tal1* (ISH), and DTg precursors co-express Foxo1 and Pax3 (IHC). The two populations are distinct, as demonstrated by IHC for Zfpm2 and Pax3. White arrowheads indicate single-positive cells, and yellow arrowheads indicate double-positive cells.

(legend continued on next page)

Altogether, our results suggested that the medial rV2 gives rise to a unique subtype of Tal1-dependent *Sall3*$^{+}$ GABAergic neurons located in the proximity of DR serotonergic neurons.

Development of the VTg, DTg, and pSNpr from Distinct r1 Precursors

Having identified genes expressed in subgroups of Tal1-dependent and independent GABAergic precursors during early development, we asked how they correspond to the GABAergic neuron subtypes and nuclei in the perinatal brain. By ISH and IHC, we followed the expression of a Tal1-dependent marker, *Zfpm2* (rV2 GABAergic clusters 40, 4, 19, 6, and 7), and a Tal1-independent marker, *Foxo1* (lateral GABAergic cluster 11), during the development of r1 from E12.5 to E15.5 (Figure 6A). At E12.5, Zfpm2^{+} cells (co-expressing *Tal1*) were located in the rV2 domain, while Foxo1^{+} precursors (co-expressing *Otp* and *Pax3*) were more dorsal. At E15.5, both populations were located near the midline, with Foxo1^{+} precursors positioned dorsally and Zfpm2^{+} cells more ventrally. Analyses of E18.5 and adult brain demonstrated that Zfpm2 and Foxo1 labeled the VTg and DTg, respectively (Figures 6B and 6C). Zfpm2 co-localized with Pvalb in the VTg, including its ventral part marked by Calb1-expressing fibers (Dillingham et al., 2015). Foxo1^{+} cells did not express Pvalb but were intermingled with Pvalb^{+} cells in the DTg. To confirm the distinct developmental origins of the VTg and DTg, we performed genetic fate mapping with *Pax7*^{Cre}, which labels cells derived from alar plate progenitors. In E18.5 *Pax7*-^{Cre};*R26R*^{TdTomato} embryos, Foxo1^{+} DTg cells expressed RFP, while Zfpm2^{+} VTg cells were not labeled, confirming the distinct developmental origins of these nuclei (Figure S5A). To birth-date the Zfpm2^{+} VTg and Foxo1^{+} DTg neurons, we injected pregnant females at E10.5–E13.5 with 5-ethynyl-2′-deoxyuridine (EdU) or 5-bromo-2'-deoxyuridine (BrdU) and analyzed cellular DNA labeling together with Zfpm2 and Foxo1 expression at postnatal day 0.5 (P0.5) (Figures S5B and S5C). Approximately 70% of both Foxo1^{+} DTg and Zfpm2^{+} VTg cells were generated between E10.5 and E11.5, but Zfpm2^{+} VTg cells were produced for a longer developmental period (Figure S5D). In summary, the VTg and DTg show differences in their gene expression, developmental origins, and timing of neurogenesis.

In addition to the VTg, Zfpm2 has been shown to be expressed in the SNpr (Lahti et al., 2016). The expression of Pax5, another TF marking Tal1-dependent GABAergic precursors, was recently also detected in the SNpr (Saunders et al., 2018; Zeisel et al., 2018). Therefore, we compared the expression of *Zfpm2* and *Pax5* at different embryonic time points. At E12.5, Pax5 was expressed in Zfpm2^{+} cells in the anterior r1, while Zfpm2^{+} cells in the posterior r1 did not express Pax5 (Figure S6A). At E15.5, we observed two Zfpm2^{+} populations, Zfpm2^{+};Pax5^{+} cells in the developing pSNpr and Zfpm2^{+};Pax5^{-} cells in the presumptive VTg, suggesting that the Zfpm2^{+} populations in the anterior and posterior r1 give rise to different nuclei (Figure S6B). At E18.5, the expression of *Pax5* was maintained in the SNpr, where *Pax5* co-localized with *Zfpm2*, *En1*, and *Ctip2*, markers of pSNpr neurons (Lahti et al., 2016; Allen Brain Atlas), but not with *Six3* and *Foxp1*, markers of the anterior SNpr (aSNpr), which has a different developmental origin (Figure S6C) (Lahti et al., 2016). Moreover, our data suggest that r1-derived Pax5^{+} pSNpr neurons are intermingled with aSNpr neurons in a gradient established late in embryonic development and not apparent at E14.5 (Figures S6 and S7B).

In summary, these results suggest that alar-plate-derived Foxo1^{+} precursors give rise to DTg GABAergic neurons, whereas VTg and SNpr GABAergic neurons diverge from Zfpm2^{+} rV2 GABAergic precursors.

Regulation of GABAergic Neuron Differentiation by Zfpm2 and Sox14, TFs Activated Downstream of Tal1

Finally, we examined the requirement for Tal1 and its downstream genes, *Sox14* and *Zfpm2*, in the development of r1-derived tegmental nuclei, including the VTg, DTg, RMTg, LDTg, and SNpr, using *Tal1*^{cko}, *En1*^{Cre};*Zfpm2*$^{flox/flox}$ (*Zfpm2*^{cko}) and *Sox14*$^{gfp/gfp}$ mouse mutants. In contrast to *Tal1*^{cko} embryos (Lahti et al., 2016), early GABAergic precursor production appeared normal in E12.5 *Zfpm2*^{cko} and *Sox14*$^{gfp/gfp}$ embryos, as we did not observe changes in expression of GABAergic and glutamatergic markers (e.g., *Gad1*, *Tal1*, *FoxP1*, Vsx2, and Nkx6-1; data not shown). As we had shown that the Zfpm2^{+} and Tal1^{+} VTg neurons were derived from GABAergic precursor clusters that also expressed Sox14, we analyzed VTg development in all of these mutants at E18.5/P0.5 using ISH or IHC for Zfpm2, *Tal1*, and *Gad1* (Figure 7A). In *Zfpm2*^{cko} and *Tal1*^{cko} mice, VTg neurons were almost completely lost. The few remaining VTg cells in the *Zfpm2*^{cko} were likely due to incomplete recombination, as all the VTg neurons appear r1 derived (Figure S5E). In *Sox14*$^{gfp/gfp}$ mutants, the VTg developed normally, indicating that in contrast to Tal1 and Zfpm2, Sox14 is not required for the differentiation of the VTg cells. Consistent with the distinct origins of VTg and DTg neurons, we found the Foxo1^{+} DTg unaltered in all of these mutants (Figure 7A).

In *Tal1*^{cko} mice, rV2-derived GABAergic neurons in the RMTg and pSNpr are lost, while the number of glutamatergic neurons in the LDTg is increased (Lahti et al., 2016). Similar to *Tal1*^{cko} mice, the development of the RMTg was impaired in both the *Zfpm2*^{cko} and *Sox14*$^{gfp/gfp}$ brains at E18.5/P0.5, as demonstrated by reduced numbers of neurons expressing the RMTg markers *Gad1*, Sox2, and FoxP1 (FoxP1: *Ctrl* versus *Zfpm2*^{cko}, $p < 0.001$, *Ctrl* versus *Sox14*$^{gfp/gfp}$, $p < 0.001$) (Figures 7B and S7A). Further resembling *Tal1*^{cko} mice, the number of pSNpr (Ctip2^{+}) neurons was significantly reduced in *Zfpm2*^{cko} mice (Ctip2: *Ctrl* versus *Zfpm2*^{cko}, $p < 0.001$), but in *Sox14*$^{gfp/gfp}$ mice, pSNpr markers were unaffected (Figure 7C and S7B). In both *Zfpm2*^{cko} and *Sox14*$^{gfp/gfp}$ mice, the aSNpr developed normally (Figure 7C), reflecting the distinct developmental origins

(B) Zfpm2 and Foxo1 expression in the E18.5 VTg and DTg (IHC).
(C) Zfpm2 and Foxo1 expression in the adult VTg and DTg (IHC). Zfpm2 is detected in Pvalb^{+} VTg cells, but not in the DTg. In the VTg, Zfpm2^{+} cells are also found in the area containing Calb1^{+} fibers. Foxo1 is expressed in the DTg, but not in its Pvalb^{+} neurons. In close-ups of the boxed areas, white arrowheads indicate single-positive cells, and yellow arrowheads indicate double-positive cells. VTg, ventral tegmental nucleus of Gudden; DTg, dorsal tegmental nucleus of Gudden. Scale bars represent 100 μm (A and B), 50 μm (C), and 20 μm (close-up). See also Figure S5.

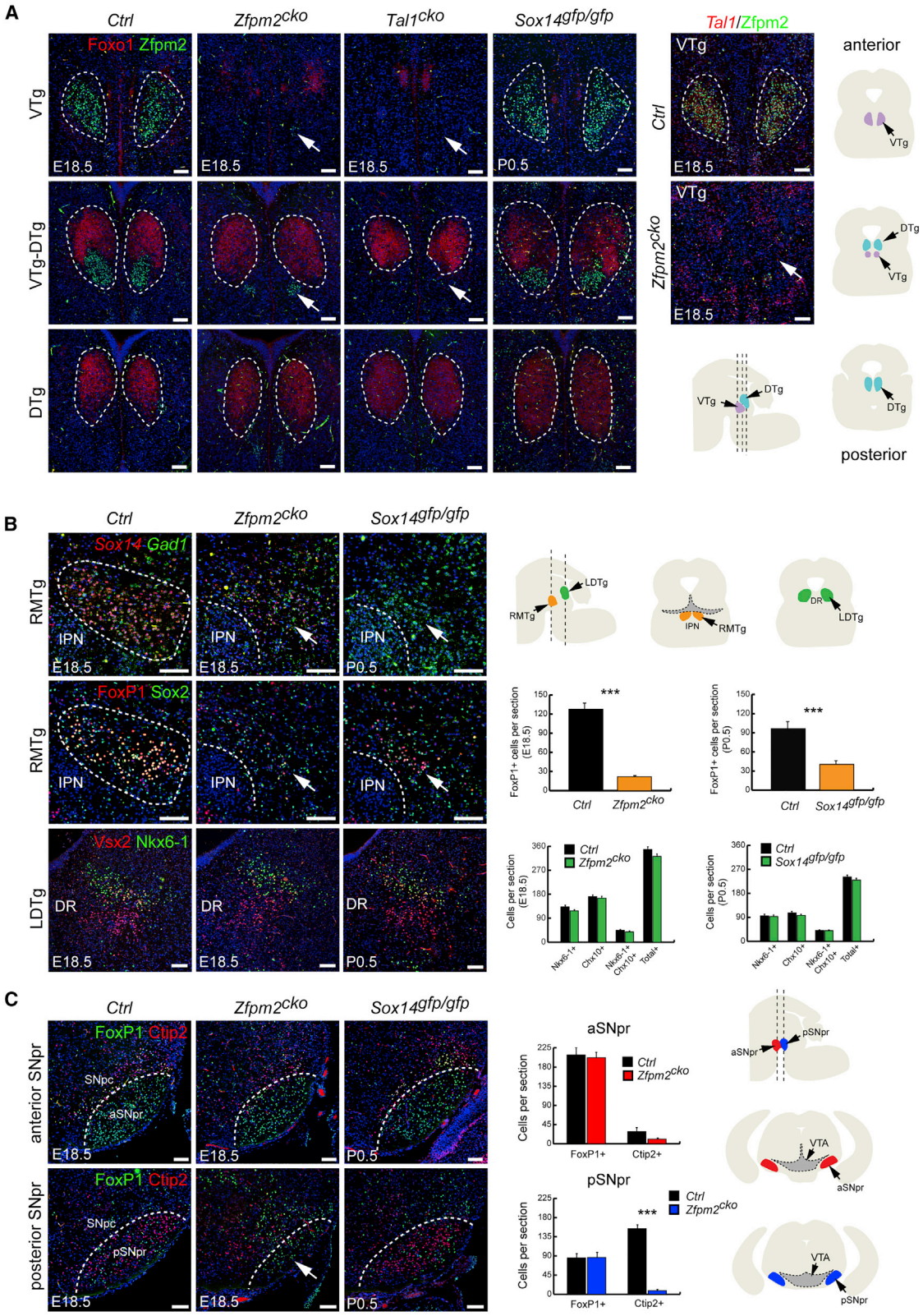

(legend on next page)

and regulation of the aSNpr and pSNpr (Lahti et al., 2016). In contrast to *Tal1*^{cko} mice, we did not observe an increase in glutamatergic Vsx2^{+} or Nkx6-1^{+} LDTg neurons in *Zfpm2*^{cko} and *Sox14*$^{gfp/gfp}$ mutants (Figure 7B).

Altogether, our results suggest that Tal1, Zfpm2, and Sox14 are differently required for the development of ventral-r1-derived nuclei. Whereas Tal1 acts in early precursors and regulates the choice between GABAergic and glutamatergic fates, Zfpm2 and Sox14 are expressed downstream of Tal1 in the differentiating GABAergic precursors and are required for later development the distinct subtypes of GABAergic neurons in the VTg, RMTg, and pSNpr.

DISCUSSION

Knowledge of the neuronal cell types in the anterior brainstem is fundamental for understanding the regulation of mood, motivation, and movement. We applied single-cell transcriptomics to profile neuronal precursors in the ventral embryonic r1, a source of tegmental GABAergic and glutamatergic neurons. As the TF Tal1 regulates differentiation of brainstem GABAergic neuron subtypes, a special emphasis was to uncover the heterogeneity of the Tal1-dependent precursors. We found an intricate developmental sequence of the GABAergic and glutamatergic precursor segregation in the ventral r1, demonstrated a role for Notch signaling in this process, and identified molecular markers of the tegmental GABAergic neuron subtypes (for additional visualization of gene expression in the single-cell data, see http://tegex.helsinki.fi/). Moreover, we demonstrated requirements for Zfpm2 and Sox14, two TFs downstream of Tal1, in the differentiation of GABAergic neurons in specific tegmental nuclei.

Early Differentiation and Bifurcation of the GABAergic and Glutamatergic Lineages in the Ventral r1

Balanced differentiation of GABAergic and glutamatergic neurons in the ventral r1 is essential for the correct development of tegmental nuclei and normal behavior (Lahti et al., 2016; Morello et al., 2020). Our study unravels complex gene expression changes associated with different steps of GABAergic neuron differentiation in the ventral r1. Many of the genes expressed in early GABAergic precursors encode for TFs, such as Insm2 and St18. These TFs may regulate general events during the cell-cycle exit and neuronal differentiation, as shown for their paralogs during cortical neurogenesis (Matsushita et al., 2014; Tavano et al., 2018; Vasconcelos et al., 2016).

The genes activated early during the post-mitotic differentiation also include putative regulators of GABAergic differentiation. The Notch signaling pathway regulates the balance between GABAergic and glutamatergic neuron differentiation of the p2 progenitors giving rise to V2a and V2b neurons in the ventral spinal cord (Del Barrio et al., 2007; Okigawa et al., 2014; Peng et al., 2007). We found that also in the rV2, asymmetry of Notch signaling was established in early post-mitotic precursors. Our analysis of *Psen1*$^{-/-}$ mice supports the conclusion that Notch signaling is required for selection between the GABAergic and glutamatergic differentiation programs in rV2 precursors. Further quantification of all the cell types derived from the rV2 region in *Ctrl* versus *Psen1*$^{-/-}$ animals, as well as measurements of the activity of individual Notch signaling pathway members in rV2 progenitors and precursors, would be required to pinpoint the biological mechanism of the cell-fate selection process. As a starting point, our computational analyses of the single-cell RNA-sequencing data provide hints for the putative molecular players in cell-fate selection. Notch target genes, such as *Hes5* and *Hey*, were expressed in early rV2 GABAergic precursors. In contrast, early rV2 glutamatergic precursors expressed the Notch ligand genes *Dll3* and *Dll4* as well as *Hes6*. Thus, directional Notch signaling and mutual antagonism between *Hes5* and *Hes6* (Fior and Henrique, 2005) may contribute to lineage segregation. Furthermore, the glutamatergic branch TFs Mybl1, Nhlh1, Cbfa2t2, and Ebf2 are repressed by intracellular Notch signaling; suppress Notch-induced transcription; or positively control Dll expression (Dubois et al., 1998; Kaufman et al., 2019; Parang et al., 2015; Ratié et al., 2013). On the other hand, TFs expressed in the GABAergic branch, such as Cbfa2t3 (Eto2/MTG16), cooperate with Tal1 and Notch function (Chagraoui et al., 2018; Engel et al., 2010).

Our results also imply a role for additional regulators of the Notch pathway. These include a cargo protein, Pdzk1ip1, recently shown to interact with Numb and promote Notch activity (Garcia-Heredia et al., 2017). Noteworthy, the *Pdzk1ip1* gene is located next to *Tal1* on chromosome 4, and the two genes share enhancer elements in hematopoietic cells (Delabesse et al., 2005; Tijssen et al., 2011; Zhou et al., 2013). Our results suggest that the initial activation of *Tal1* and *Pdzk1ip1* occurs in parallel, possibly also driven by a shared enhancer in differentiating

Figure 7. Requirement for Zfpm2 and Sox14 in the Development of rV2 GABAergic Neuron Subtypes

(A) Expression of DTg and VTg markers in *Ctrl*, *Zfpm2*^{cko}, *Tal1*^{cko}, and *Sox14*$^{gfp/gfp}$ mice at E18.5/P0.5 (IHC and ISH). In *Zfpm2*^{cko} and *Tal1*^{cko} mice, most Zfpm2^{+}/Tal1^{+} VTg cells are lost (arrows), while development of the Foxo1^{+} DTg is normal. Analysis of *Tal1* and Zfpm2 expression showing *Tal1* co-localization with Zfpm2 in the VTg in *Ctrl* mice and loss of expression of both markers in *Zfpm2*^{cko} mice (arrow).

(B) Expression of RMTg and LDTg markers in *Zfpm2*^{cko} and *Sox14*$^{gfp/gfp}$ mice at E18.5/P0.5 (ISH and IHC), showing downregulation of the RMTg markers *Sox14*, FoxP1, and Sox2 (arrows); expression of the LDTg markers Vsx2 and Nkx6-1 is not affected. Quantification of FoxP1^{+} cells in the RMTg of *Zfpm2*^{cko} and *Sox14*$^{gfp/gfp}$ animals (cells/section). *Ctrl* versus *Zfpm2*^{cko} (E18.5), ***$p < 0.001$ (non-parametric Mann-Whitney *U* test). *Ctrl* versus *Sox14*$^{gfp/gfp}$ (P0), ***$p < 0.001$ (non-parametric Mann-Whitney *U* test). Quantification of Vsx2^{+}, Nkx6-1^{+}, Vsx2^{+}Nkx6-1^{+}, and Vsx2^{+} or Nkx6-1^{+} (total) cells in the LDTg of *Zfpm2*^{cko} and *Sox14*$^{gfp/gfp}$ animals (cells/section). *Ctrl* versus *Zfpm2*^{cko} (E18.5), $p > 0.05$ (non-parametric Mann-Whitney *U* test). *Ctrl* versus *Sox14*$^{gfp/gfp}$ (P0), $p > 0.05$ (non-parametric Mann-Whitney *U* test). Bars represent the mean ± SEM. IPN, interpeduncular nucleus.

(C) Expression of SNpr markers in *Zfpm2*^{cko} and *Sox14*$^{gfp/gfp}$ mice at E18.5/P0.5 (IHC). In both mutants, the FoxP1^{+} aSNpr develops normally. The development of Ctip2^{+} pSNpr is impaired in *Zfpm2*^{cko} mice. Quantification of FoxP1^{+} and Ctip2^{+} cells in the aSNpr and pSNpr of *Zfpm2*^{cko} animals (cells/section) is shown. *Ctrl* versus *Zfpm2*^{cko} (E18.5): aSNpr, $p > 0.05$ (non-parametric Mann-Whitney *U* test); pSNpr, $p > 0.05$ (FoxP1^{+}) (Student's t test) and ***$p < 0.001$ (Ctip2^{+}) (non-parametric Mann-Whitney *U* test).

Error bars represent mean ± SEM. Scale bars represent 100 μm. See also Figures S5–S7.

neural precursors. As *Pdzk1ip1* is normally rapidly downregulated in differentiating GABAergic precursors, the increase in its expression in the *Tal1* mutant brain may indicate a delay in the developmental progression of GABAergic precursors, before their redirection into a glutamatergic identity. Our results also suggest that Ttyh1, recently shown to promote γ-secretase activity and Notch intracellular domain production (Kim et al., 2018), is a potential intracellular stimulator of Notch signaling in early GABAergic precursors. Furthermore, analysis of lineage-specific gene expression indicates reciprocal pathways, involving Angpt1 and Sstr2, in signaling from GABAergic to glutamatergic precursors during lineage branching. Notably, in angiogenic blood vessels, Angpt1 stimulates *Dll4* expression (Shah et al., 2017). Interconnected Notch and Angpt1 signaling may similarly regulate the balance between GABAergic and glutamatergic differentiation in the ventral r1.

Development of Tegmental GABAergic Neuron Diversity

Our work demonstrates that the functionally diverse tegmental GABAergic neurons have different embryonic origins and are characterized by subtype-specific TFs required for the development of tegmental nuclei. For example, the main GABAergic neuron subtypes in the VTg and DTg, nuclei with rather similar projection patterns but distinct functions in memory and navigation (Vann and Nelson, 2015), are derived from the rV2 and lateral r1, respectively. Within the Tal1 lineage, we also discovered subgroups of GABAergic precursors and identified Tal1-dependent TFs marking them. We found that the TFs Zfpm2 and Sox14 were important for the full maturation of tegmental GABAergic neuron subtypes. In the case of Zfpm2, this may involve direction of the Gata/Tal TF complex to specific genomic loci, as its homolog, Zfpm1, modulates the DNA binding of Gata factors in hematopoietic cells (Chlon et al., 2012). Sox14 expression in developing thalamic and midbrain GABAergic precursors is Gata2 dependent, but, instead of a Gata2-dependent GABAergic identity, Sox14 is required for the migration of GABAergic precursors to thalamic nuclei (Delogu et al., 2012; Jager et al., 2016; Virolainen et al., 2012). The role of Sox14 may be similar in the developing RMTg, as unlike the loss of Tal1, the loss of Sox14 function did not result in a GABAergic to glutamatergic fate transformation. We found that Sox21, a Sox14-related TF, is also expressed in rV2 precursors. Partial redundancy between these factors, due to shared and unique cell types expressing them, may contribute to selective requirements for Sox14 in GABAergic and glutamatergic precursors.

The diversity within the Tal1 lineage may also reflect antero-posterior and dorsoventral regionalization of the rV2. For example, anterior Tal1$^+$;Zfpm2$^+$;Pax5$^+$ precursors appear to migrate to the pSNpr, while the more posterior Tal1$^+$;Zfpm2$^+$;Pax5$^-$ cells localize to the VTg. *Pax5* expression in anterior rV2 precursors may reflect progenitor patterning by isthmic-organizer-derived signals (Urbánek et al., 1997). Consistent with our results, recent large-scale single-cell transcriptomic studies of adult brain found Tal1$^+$;Pax5$^+$;Zfpm2$^+$ GABAergic neurons in the SNpr (Saunders et al., 2018; Zeisel et al., 2018). Further subtypes of pSNpr neurons were also distinguished (Lahti et al., 2016; Saunders et al., 2018). Although not all of these were found in our data, our results suggest that the main tegmental GABAergic neuron subtypes, or at least their markers, can be identified in early embryonic precursors. In addition to antero-posterior differences, we identified a subtype of Tal1-dependent *Sall3*$^+$ GABAergic precursors in the medial (ventral) rV2 and found that they migrate next to the serotonergic neurons in the DR, marking a region that does not correlate with a previously identified brain nucleus. Interestingly, GABAergic neurons around the DR participate in the regulation of serotonergic neurons and control movement during avoidance behavior (Challis et al., 2013; Seo et al., 2019). In addition to spatial patterning, temporal changes in progenitors may contribute to the generation of neuronal diversity (Delile et al., 2019). However, we observed early activation of the subtype-specific TFs, suggesting that GABAergic and glutamatergic neurons are produced from the onset of neurogenesis in the rV2.

Conclusions

Transcriptional profiling of embryonic neuronal precursors in the r1 revealed developmental pathways and molecular characteristics of tegmental neurons. We identified several subtype-specific TFs important for development of the brainstem GABAergic nuclei. We provide a frame of reference for embryonic origins and diversity of GABAergic and glutamatergic neurons in the tegmental nuclei, in particular in the SNpr, RMTg, LDTg, VTg, and DTg and the DR region. Targets of these neurons include the monoaminergic nuclei, and they form integral parts of circuits that regulate voluntary movement, motivation, and learning.

STAR★METHODS

Detailed methods are provided in the online version of this paper and include the following:

- KEY RESOURCES TABLE
- RESOURCE AVAILABILITY
  - Lead Contact
  - Materials Availability
  - Data and Code availability
- EXPERIMENTAL MODEL AND SUBJECT DETAILS
  - Animals
- METHOD DETAILS
  - Histology
  - Immunohistochemistry
  - mRNA *in situ* hybridization
  - EdU and BrdU labeling
  - Stereotaxic surgery and neuronal labeling
  - Imaging
  - RNA sequencing
  - Read mapping and expression quantification
  - Differential expression analysis
  - Validation of selected differentially expressed genes by RT-qPCR
  - Single-cell mRNA sequencing
  - Processing of the single-cell mRNA sequencing reads
  - Clustering analyses of the single-cell mRNA sequencing data
  - Comparison of the E12.5 and E13.5 cell clusters
  - Developmental trajectory (pseudotime) analyses
- QUANTIFICATION AND STATISTICAL ANALYSIS

SUPPLEMENTAL INFORMATION

Supplemental Information can be found online at https://doi.org/10.1016/j.celrep.2020.108268.

ACKNOWLEDGMENTS

We acknowledge Outi Kostia and Anniina Tervi for excellent technical assistance, Lassi Virtanen and Sami Kilpinen for building the tegex website, and thank Flora Vaccarino (Otp antibody), Joshua R. Sanes (NeuroD6 probe), Toshiki Kameyama (St18 probe), Domna Karagogeos (Cntn2 probe), and Qiufu Ma (Tlx3 probe) for reagents. L.T. was funded by the Integrative Life Science doctoral program. P.T. was supported by Helsinki Institute of Life Science. This work was supported by the Academy of Finland, Sigrid Juselius Foundation, and Jane and Aatos Erkko Foundation.

AUTHOR CONTRIBUTIONS

L.T., L.L., F.M., and K.A. prepared the samples for single-cell and bulk mRNA sequencing. M. Survila and L.M. set up the InDrop method, prepared the single-cell mRNA sequencing libraries, and analyzed the data. D.B., S.S.-O., P.T., and K.A. carried out the bioinformatic analyses. F.M., L.T., L.L., N.E., L.K., A.D., and K.A. validated the data analyzing gene expression in the control and mutant mouse tissues. A.K. performed the retrograde tracing experiments. M. Salminen and J.P. supervised the project and participated in the analyses of the results. All the authors contributed to writing the manuscript.

DECLARATION OF INTERESTS

The authors declare no competing interests.

Received: February 4, 2019
Revised: June 9, 2020
Accepted: September 22, 2020
Published: October 13, 2020

REFERENCES

Achim, K., Peltopuro, P., Lahti, L., Li, J., Salminen, M., and Partanen, J. (2012). Distinct developmental origins and regulatory mechanisms for GABAergic neurons associated with dopaminergic nuclei in the ventral mesodiencephalic region. Development *139*, 2360–2370.

Anders, S., McCarthy, D.J., Chen, Y., Okoniewski, M., Smyth, G.K., Huber, W., and Robinson, M.D. (2013). Count-based differential expression analysis of RNA sequencing data using R and Bioconductor. Nat. Protoc. *8*, 1765–1786.

Aroca, P., Lorente-Cánovas, B., Mateos, F.R., and Puelles, L. (2006). Locus coeruleus neurons originate in alar rhombomere 1 and migrate into the basal plate: studies in chick and mouse embryos. J. Comp. Neurol. *496*, 802–818.

Barrot, M., Sesack, S.R., Georges, F., Pistis, M., Hong, S., and Jhou, T.C. (2012). Braking dopamine systems: a new GABA master structure for mesolimbic and nigrostriatal functions. J. Neurosci. *32*, 14094–14101.

Becht, E., McInnes, L., Healy, J., Dutertre, C.-A., Kwok, I.W.H., Ng, L.G., Ginhou, F., and Newell, E.W. (2018). Dimensionality reduction for visualizing single-cell data using UMAP. Nat Biotechnol. https://doi.org/10.1038/nbt.4314.

Benjamini, Y., and Hochberg, Y. (1995). Controlling the false discovery rate: a practical and powerful approach to multiple testing. J. R. Stat. Soc. B Met. *57*, 289–300.

Blondel, V.D., Guillaume, J.L., Lambiotte, R., and Lefebvre, E. (2008). Fast unfolding of communities in large networks. J. Stat. Mech. Theory E. *2008*, P10008.

Bolger, A.M., Lohse, M., and Usadel, B. (2014). Trimmomatic: a flexible trimmer for Illumina sequence data. Bioinformatics *30*, 2114–2120.

Bradley, C.K., Takano, E.A., Hall, M.A., Göthert, J.R., Harvey, A.R., Begley, C.G., and van Eekelen, J.A. (2006). The essential haematopoietic transcription factor Scl is also critical for neuronal development. Eur. J. Neurosci. *23*, 1677–1689.

Brown, J., Pan, W.X., and Dudman, J.T. (2014). The inhibitory microcircuit of the substantia nigra provides feedback gain control of the basal ganglia output. eLife *3*, e02397.

Canzoniere, D., Farioli-Vecchioli, S., Conti, F., Ciotti, M.T., Tata, A.M., Augusti-Tocco, G., Mattei, E., Lakshmana, M.K., Krizhanovsky, V., Reeves, S.A., et al. (2004). Dual control of neurogenesis by PC3 through cell cycle inhibition and induction of Math1. J. Neurosci. *24*, 3355–3369.

Chagraoui, H., Kristiansen, M.S., Ruiz, J.P., Serra-Barros, A., Richter, J., Hall-Ponselé, E., Gray, N., Waithe, D., Clark, K., Hublitz, P., et al. (2018). SCL/TAL1 cooperates with Polycomb RYBP-PRC1 to suppress alternative lineages in blood-fated cells. Nat. Commun. *9*, 5375.

Chakrabarty, K., Von Oerthel, L., Hellemons, A., Clotman, F., Espana, A., Groot Koerkamp, M., Holstege, F.C., Pasterkamp, R.J., and Smidt, M.P. (2012). Genome wide expression profiling of the mesodiencephalic region identifies novel factors involved in early and late dopaminergic development. Biol. Open *1*, 693–704.

Challis, C., Boulden, J., Veerakumar, A., Espallergues, J., Vassoler, F.M., Pierce, R.C., Beck, S.G., and Berton, O. (2013). Raphe GABAergic neurons mediate the acquisition of avoidance after social defeat. J. Neurosci. *33*, 13978–13988.

Cheng, L., Samad, O.A., Xu, Y., Mizuguchi, R., Luo, P., Shirasawa, S., Goulding, M., and Ma, Q. (2005). Lbx1 and Tlx3 are opposing switches in determining GABAergic versus glutamatergic transmitter phenotypes. Nat. Neurosci. *8*, 1510–1515.

Chlon, T.M., and Crispino, J.D. (2012). Combinatorial regulation of tissue specification by GATA and FOG factors. Development *139*, 3905–3916.

Chlon, T.M., Doré, L.C., and Crispino, J.D. (2012). Cofactor-mediated restriction of GATA-1 chromatin occupancy coordinates lineage-specific gene expression. Mol. Cell *47*, 608–621.

Davis, C.A., and Joyner, A.L. (1988). Expression patterns of the homeo box-containing genes En-1 and En-2 and the proto-oncogene int-1 diverge during mouse development. Genes Dev. *2* (*12B*), 1736–1744.

De Strooper, B., Saftig, P., Craessaerts, K., Vanderstichele, H., Guhde, G., Annaert, W., Von Figura, K., and Van Leuven, F. (1998). Deficiency of presenilin-1 inhibits the normal cleavage of amyloid precursor protein. Nature *391*, 387–390.

Del Barrio, M.G., Taveira-Marques, R., Muroyama, Y., Yuk, D.I., Li, S., Wines-Samuelson, M., Shen, J., Smith, H.K., Xiang, M., Rowitch, D., and Richardson, W.D. (2007). A regulatory network involving Foxn4, Mash1 and delta-like 4/Notch1 generates V2a and V2b spinal interneurons from a common progenitor pool. Development *134*, 3427–3436.

Delabesse, E., Ogilvy, S., Chapman, M.A., Piltz, S.G., Gottgens, B., and Green, A.R. (2005). Transcriptional regulation of the SCL locus: identification of an enhancer that targets the primitive erythroid lineage in vivo. Mol. Cell. Biol. *25*, 5215–5225.

Delile, J., Rayon, T., Melchionda, M., Edwards, A., Briscoe, J., and Sagner, A. (2019). Single cell transcriptomics reveals spatial and temporal dynamics of gene expression in the developing mouse spinal cord. Development *146*, 146.

Delogu, A., Sellers, K., Zagoraiou, L., Bocianowska-Zbrog, A., Mandal, S., Guimera, J., Rubenstein, J.L., Sugden, D., Jessell, T., and Lumsden, A. (2012). Subcortical visual shell nuclei targeted by ipRGCs develop from a Sox14+-GABAergic progenitor and require Sox14 to regulate daily activity rhythms. Neuron *75*, 648–662.

Denaxa, M., Chan, C.H., Schachner, M., Parnavelas, J.G., and Karagogeos, D. (2001). The adhesion molecule TAG-1 mediates the migration of cortical interneurons from the ganglionic eminence along the corticofugal fiber system. Development *128*, 4635–4644.

Dillingham, C.M., Holmes, J.D., Wright, N.F., Erichsen, J.T., Aggleton, J.P., and Vann, S.D. (2015). Calcium-binding protein immunoreactivity in Gudden's tegmental nuclei and the hippocampal formation: differential co-localization in neurons projecting to the mammillary bodies. Front. Neuroanat. *9*, 103.

Dobin, A., Davis, C.A., Schlesinger, F., Drenkow, J., Zaleski, C., Jha, S., Batut, P., Chaisson, M., and Gingeras, T.R. (2013). STAR: ultrafast universal RNA-seq aligner. Bioinformatics *29*, 15–21.

Dubois, L., Bally-Cuif, L., Crozatier, M., Moreau, J., Paquereau, L., and Vincent, A. (1998). XCoe2, a transcription factor of the Col/Olf-1/EBF family involved in the specification of primary neurons in Xenopus. Curr. Biol. *8*, 199–209.

Engel, M.E., Nguyen, H.N., Mariotti, J., Hunt, A., and Hiebert, S.W. (2010). Myeloid translocation gene 16 (MTG16) interacts with Notch transcription complex components to integrate Notch signaling in hematopoietic cell fate specification. Mol. Cell. Biol. *30*, 1852–1863.

Fior, R., and Henrique, D. (2005). A novel hes5/hes6 circuitry of negative regulation controls Notch activity during neurogenesis. Dev. Biol. *281*, 318–333.

Funato, H., Sato, M., Sinton, C.M., Gautron, L., Williams, S.C., Skach, A., Elmquist, J.K., Skoultchi, A.I., and Yanagisawa, M. (2010). Loss of Goosecoid-like and DiGeorge syndrome critical region 14 in interpeduncular nucleus results in altered regulation of rapid eye movement sleep. Proc. Natl. Acad. Sci. USA *107*, 18155–18160.

Gao, X., Hu, D., Gogol, M., and Li, H. (2019). ClusterMap: compare multiple single cell RNA-Seq datasets across different experimental conditions. Bioinformatics *35*, 3038–3045.

Garcia-Heredia, J.M., Lucena-Cacace, A., Verdugo-Sivianes, E.M., Pérez, M., and Carnero, A. (2017). The Cargo Protein MAP17 (PDZK1IP1) Regulates the Cancer Stem Cell Pool Activating the Notch Pathway by Abducting NUMB. Clin. Cancer Res. *23*, 3871–3883.

Green, M.J., and Wingate, R.J. (2014). Developmental origins of diversity in cerebellar output nuclei. Neural Dev. *9*, 1.

Guimera, J., Weisenhorn, D.V., and Wurst, W. (2006). Megane/Heslike is required for normal GABAergic differentiation in the mouse superior colliculus. Development *133*, 3847–3857.

Haugas, M., Tikker, L., Achim, K., Salminen, M., and Partanen, J. (2016). Gata2 and Gata3 regulate the differentiation of serotonergic and glutamatergic neuron subtypes of the dorsal raphe. Development *143*, 4495–4508.

Jager, P., Ye, Z., Yu, X., Zagoraiou, L., Prekop, H.T., Partanen, J., Jessell, T.M., Wisden, W., Brickley, S.G., and Delogu, A. (2016). Tectal-derived interneurons contribute to phasic and tonic inhibition in the visual thalamus. Nat. Commun. *7*, 13579.

Joshi, K., Lee, S., Lee, B., Lee, J.W., and Lee, S.K. (2009). LMO4 controls the balance between excitatory and inhibitory spinal V2 interneurons. Neuron *61*, 839–851.

Kameyama, T., Matsushita, F., Kadokawa, Y., and Marunouchi, T. (2011). Myt/NZF family transcription factors regulate neuronal differentiation of P19 cells. Neurosci. Lett. *497*, 74–79.

Kaufman, M.L., Park, K.U., Goodson, N.B., Chew, S., Bersie, S., Jones, K.L., Lamba, D.A., and Brzezinski, J.A., 4th. (2019). Transcriptional profiling of murine retinas undergoing semi-synchronous cone photoreceptor differentiation. Dev. Biol. *453*, 155–167.

Kay, J.N., Voinescu, P.E., Chu, M.W., and Sanes, J.R. (2011). Neurod6 expression defines new retinal amacrine cell subtypes and regulates their fate. Nat. Neurosci. *14*, 965–972.

Keller, C., Hansen, M.S., Coffin, C.M., and Capecchi, M.R. (2004). Pax3:Fkhr interferes with embryonic Pax3 and Pax7 function: implications for alveolar rhabdomyosarcoma cell of origin. Genes Dev. *18*, 2608–2613.

Kim, J., Han, D., Byun, S.H., Kwon, M., Cho, J.Y., Pleasure, S.J., and Yoon, K. (2018). Ttyh1 regulates embryonic neural stem cell properties by enhancing the Notch signaling pathway. EMBO Rep. *19*, e45472.

Kimmel, R.A., Turnbull, D.H., Blanquet, V., Wurst, W., Loomis, C.A., and Joyner, A.L. (2000). Two lineage boundaries coordinate vertebrate apical ectodermal ridge formation. Genes Dev. *14*, 1377–1389.

Klein, A.M., Mazutis, L., Akartuna, I., Tallapragada, N., Veres, A., Li, V., Peshkin, L., Weitz, D.A., and Kirschner, M.W. (2015). Droplet barcoding for single-cell transcriptomics applied to embryonic stem cells. Cell *161*, 1187–1201.

Lahti, L., Haugas, M., Tikker, L., Airavaara, M., Voutilainen, M.H., Anttila, J., Kumar, S., Inkinen, C., Salminen, M., and Partanen, J. (2016). Differentiation and molecular heterogeneity of inhibitory and excitatory neurons associated with midbrain dopaminergic nuclei. Development *143*, 516–529.

Lammel, S., Lim, B.K., Ran, C., Huang, K.W., Betley, M.J., Tye, K.M., Deisseroth, K., and Malenka, R.C. (2012). Input-specific control of reward and aversion in the ventral tegmental area. Nature *491*, 212–217.

Langmead, B., Trapnell, C., Pop, M., and Salzberg, S.L. (2009). Ultrafast and memory-efficient alignment of short DNA sequences to the human genome. Genome Biol. *10*, R25.

Leek, J.T., Johnson, W.E., Parker, H.S., Jaffe, A.E., and Storey, J.D. (2012). The sva package for removing batch effects and other unwanted variation in high-throughput experiments. Bioinformatics *28*, 882–883.

Lein, E.S., Hawrylycz, M.J., Ao, N., Ayres, M., Bensinger, A., Bernard, A., Boe, A.F., Boguski, M.S., Brockway, K.S., Byrnes, E.J., et al. (2007). Genome-wide atlas of gene expression in the adult mouse brain. Nature *445*, 168–176.

Liao, Y., Smyth, G.K., and Shi, W. (2014). featureCounts: an efficient general purpose program for assigning sequence reads to genomic features. Bioinformatics *30*, 923–930.

Lilleväli, K., Matilainen, T., Karis, A., and Salminen, M. (2004). Partially overlapping expression of Gata2 and Gata3 during inner ear development. Dev. Dyn. *231*, 775–781.

Lorente-Cánovas, B., Marín, F., Corral-San-Miguel, R., Hidalgo-Sánchez, M., Ferrán, J.L., Puelles, L., and Aroca, P. (2012). Multiple origins, migratory paths and molecular profiles of cells populating the avian interpeduncular nucleus. Dev. Biol. *361*, 12–26.

Lun, A.T., Bach, K., and Marioni, J.C. (2016). Pooling across cells to normalize single-cell RNA sequencing data with many zero counts. Genome Biol. *17*, 75.

Machold, R., and Fishell, G. (2005). Math1 is expressed in temporally discrete pools of cerebellar rhombic-lip neural progenitors. Neuron *48*, 17–24.

Madisen, L., Zwingman, T.A., Sunkin, S.M., Oh, S.W., Zariwala, H.A., Gu, H., Ng, L.L., Palmiter, R.D., Hawrylycz, M.J., Jones, A.R., et al. (2010). A robust and high-throughput Cre reporting and characterization system for the whole mouse brain. Nat. Neurosci. *13*, 133–140.

Manuylov, N.L., Smagulova, F.O., and Tevosian, S.G. (2007). Fog2 excision in mice leads to premature mammary gland involution and reduced Esr1 gene expression. Oncogene *26*, 5204–5213.

Marillat, V., Sabatier, C., Failli, V., Matsunaga, E., Sotelo, C., Tessier-Lavigne, M., and Chédotal, A. (2004). The slit receptor Rig-1/Robo3 controls midline crossing by hindbrain precerebellar neurons and axons. Neuron *43*, 69–79.

Matsushita, F., Kameyama, T., Kadokawa, Y., and Marunouchi, T. (2014). Spatiotemporal expression pattern of Myt/NZF family zinc finger transcription factors during mouse nervous system development. Dev. Dyn. *243*, 588–600.

McCarthy, D.J., Campbell, K.R., Lun, A.T., and Wills, Q.F. (2017). Scater: pre-processing, quality control, normalization and visualization of single-cell RNA-seq data in R. Bioinformatics *33*, 1179–1186.

McFarlane, L., Truong, V., Palmer, J.S., and Wilhelm, D. (2013). Novel PCR assay for determining the genetic sex of mice. Sex Dev. *7*, 207–211.

Millen, K.J., Steshina, E.Y., Iskusnykh, I.Y., and Chizhikov, V.V. (2014). Transformation of the cerebellum into more ventral brainstem fates causes cerebellar agenesis in the absence of Ptf1a function. Proc. Natl. Acad. Sci. USA *111*, E1777–E1786.

Morales, M., and Margolis, E.B. (2017). Ventral tegmental area: cellular heterogeneity, connectivity and behaviour. Nat. Rev. Neurosci. *18*, 73–85.

Morello, F., Voikar, V., Parkkinen, P., Panhelainen, A., Rosenholm, M., Makkonen, A., Rantamäki, T., Piepponen, P., Aitta-Aho, T., and Partanen, J. (2020). ADHD-like behaviors caused by inactivation of a transcription factor controlling the balance of inhibitory and excitatory neuron development in the mouse anterior brainstem. Translational Psychiatry *9*, in press. https://doi.org/10.1038/s41398-020-01033-8.

Nagai, T., Aruga, J., Takada, S., Günther, T., Spörle, R., Schughart, K., and Mikoshiba, K. (1997). The expression of the mouse Zic1, Zic2, and Zic3 gene

suggests an essential role for Zic genes in body pattern formation. Dev. Biol. *182*, 299–313.

Okigawa, S., Mizoguchi, T., Okano, M., Tanaka, H., Isoda, M., Jiang, Y.J., Suster, M., Higashijima, S., Kawakami, K., and Itoh, M. (2014). Different combinations of Notch ligands and receptors regulate V2 interneuron progenitor proliferation and V2a/V2b cell fate determination. Dev. Biol. *391*, 196–206.

Parang, B., Rosenblatt, D., Williams, A.D., Washington, M.K., Revetta, F., Short, S.P., Reddy, V.K., Hunt, A., Shroyer, N.F., Engel, M.E., et al. (2015). The transcriptional corepressor MTGR1 regulates intestinal secretory lineage allocation. FASEB J. *29*, 786–795.

Peng, C.Y., Yajima, H., Burns, C.E., Zon, L.I., Sisodia, S.S., Pfaff, S.L., and Sharma, K. (2007). Notch and MAML signaling drives Scl-dependent interneuron diversity in the spinal cord. Neuron *53*, 813–827.

Proulx, C.D., Hikosaka, O., and Malinow, R. (2014). Reward processing by the lateral habenula in normal and depressive behaviors. Nat. Neurosci. *17*, 1146–1152.

Qiu, X., Mao, Q., Tang, Y., Wang, L., Chawla, R., Pliner, H.A., and Trapnell, C. (2017). Reversed graph embedding resolves complex single-cell trajectories. Nat. Methods *14*, 979–982.

Ratié, L., Ware, M., Barloy-Hubler, F., Romé, H., Gicquel, I., Dubourg, C., David, V., and Dupé, V. (2013). Novel genes upregulated when NOTCH signalling is disrupted during hypothalamic development. Neural Dev. *8*, 25.

Ratié, L., Ware, M., Jagline, H., David, V., and Dupé, V. (2014). Dynamic expression of Notch-dependent neurogenic markers in the chick embryonic nervous system. Front. Neuroanat. *8*, 158.

Ritchie, M.E., Phipson, B., Wu, D., Hu, Y., Law, C.W., Shi, W., and Smyth, G.K. (2015). limma powers differential expression analyses for RNA-sequencing and microarray studies. Nucleic Acids Res. *43*, e47.

Rose, M.F., Ahmad, K.A., Thaller, C., and Zoghbi, H.Y. (2009). Excitatory neurons of the proprioceptive, interoceptive, and arousal hindbrain networks share a developmental requirement for Math1. Proc. Natl. Acad. Sci. USA *106*, 22462–22467.

Ruiz-Reig, N., Rakotobe, M., Bethus, I., Le Menn, G., Huditz, H.I., Marie, H., Lamonerie, T., and D'Autréaux, F. (2019). Developmental Requirement of Homeoprotein Otx2 for Specific Habenulo-Interpeduncular Subcircuits. J. Neurosci. *39*, 1005–1019.

Saunders, A., Macosko, E.Z., Wysoker, A., Goldman, M., Krienen, F.M., de Rivera, H., Bien, E., Baum, M., Bortolin, L., Wang, S., et al. (2018). Molecular diversity and specializations among the cells of the adult mouse brain. Cell *174*, 1015–1030.e1016.

Seo, C., Guru, A., Jin, M., Ito, B., Sleezer, B.J., Ho, Y.Y., Wang, E., Boada, C., Krupa, N.A., Kullakanda, D.S., et al. (2019). Intense threat switches dorsal raphe serotonin neurons to a paradoxical operational mode. Science *363*, 538–542.

Serafini, T., Kennedy, T.E., Galko, M.J., Mirzayan, C., Jessell, T.M., and Tessier-Lavigne, M. (1994). The netrins define a family of axon outgrowth-promoting proteins homologous to C. elegans UNC-6. Cell *78*, 409–424.

Shah, A.V., Birdsey, G.M., Peghaire, C., Pitulescu, M.E., Dufton, N.P., Yang, Y., Weinberg, I., Osuna Almagro, L., Payne, L., Mason, J.C., et al. (2017). The endothelial transcription factor ERG mediates Angiopoietin-1-dependent control of Notch signalling and vascular stability. Nat. Commun. *8*, 16002.

Simeone, A., Acampora, D., Mallamaci, A., Stornaiuolo, A., D'Apice, M.R., Nigro, V., and Boncinelli, E. (1993). A vertebrate gene related to orthodenticle contains a homeodomain of the bicoid class and demarcates anterior neuroectoderm in the gastrulating mouse embryo. EMBO J. *12*, 2735–2747.

Tamamaki, N., Yanagawa, Y., Tomioka, R., Miyazaki, J., Obata, K., and Kaneko, T. (2003). Green fluorescent protein expression and colocalization with calretinin, parvalbumin, and somatostatin in the GAD67-GFP knock-in mouse. J. Comp. Neurol. *467*, 60–79.

Tavano, S., Taverna, E., Kalebic, N., Haffner, C., Namba, T., Dahl, A., Wilsch-Brauninger, M., Paridaen, J., and Huttner, W.B. (2018). Insm1 induces neural progenitor delamination in developing neocortex via downregulation of the adherens junction belt-specific protein Plekha7. Neuron *97*, 1299–1314.e1298.

Tijssen, M.R., Cvejic, A., Joshi, A., Hannah, R.L., Ferreira, R., Forrai, A., Bellissimo, D.C., Oram, S.H., Smethurst, P.A., Wilson, N.K., et al. (2011). Genome-wide analysis of simultaneous GATA1/2, RUNX1, FLI1, and SCL binding in megakaryocytes identifies hematopoietic regulators. Dev. Cell *20*, 597–609.

Trapnell, C., Cacchiarelli, D., Grimsby, J., Pokharel, P., Li, S., Morse, M., Lennon, N.J., Livak, K.J., Mikkelsen, T.S., and Rinn, J.L. (2014). Pseudo-temporal ordering of individual cells reveals dynamics and regulators of cell fate decisions. Nat Biotechnol. *32*, 381–386.

Urbánek, P., Fetka, I., Meisler, M.H., and Busslinger, M. (1997). Cooperation of Pax2 and Pax5 in midbrain and cerebellum development. Proc. Natl. Acad. Sci. USA *94*, 5703–5708.

van der Maaten, L., and Hinton, G. (2008). Visualizing data using t-SNE. J. Mach. Learn. Res. *9*, 2579–2605.

Vann, S.D., and Nelson, A.J. (2015). The mammillary bodies and memory: more than a hippocampal relay. Prog. Brain Res. *219*, 163–185.

Vasconcelos, F.F., Sessa, A., Laranjeira, C., Raposo, A.A.S.F., Teixeira, V., Hagey, D.W., Tomaz, D.M., Muhr, J., Broccoli, V., and Castro, D.S. (2016). MyT1 counteracts the neural progenitor program to promote vertebrate neurogenesis. Cell Rep. *17*, 469–483.

Virolainen, S.M., Achim, K., Peltopuro, P., Salminen, M., and Partanen, J. (2012). Transcriptional regulatory mechanisms underlying the GABAergic neuron fate in different diencephalic prosomeres. Development *139*, 3795–3805.

Vong, L., Ye, C., Yang, Z., Choi, B., Chua, S., Jr., and Lowell, B.B. (2011). Leptin action on GABAergic neurons prevents obesity and reduces inhibitory tone to POMC neurons. Neuron *71*, 142–154.

Waite, M.R., Skaggs, K., Kaviany, P., Skidmore, J.M., Causeret, F., Martin, J.F., and Martin, D.M. (2012). Distinct populations of GABAergic neurons in mouse rhombomere 1 express but do not require the homeodomain transcription factor PITX2. Mol. Cell. Neurosci. *49*, 32–43.

Zeisel, A., Hochgerner, H., Lonnerberg, P., Johnsson, A., Memic, F., van der Zwan, J., Haring, M., Braun, E., Borm, L.E., La Manno, G., et al. (2018). Molecular architecture of the mouse nervous system. Cell *174*, 999–1014.e1022.

Zhou, Y., Kurukuti, S., Saffrey, P., Vukovic, M., Michie, A.M., Strogantsev, R., West, A.G., and Vetrie, D. (2013). Chromatin looping defines expression of TAL1, its flanking genes, and regulation in T-ALL. Blood *122*, 4199–4209.

Zilionis, R., Nainys, J., Veres, A., Savova, V., Zemmour, D., Klein, A.M., and Mazutis, L. (2017). Single-cell barcoding and sequencing using droplet microfluidics. Nat. Protoc. *12*, 44–73.

STAR★METHODS

KEY RESOURCES TABLE

REAGENT or RESOURCE	SOURCE	IDENTIFIER
Antibodies		
rabbit anti-Foxo1	Cell Signaling Technology	Cat#2880; RRID: AB_2106495
rabbit anti-Zfpm2	Santa Cruz Biotechnology	Cat#sc-10755; RRID: AB_2218978
mouse anti-Zfpm2	Santa Cruz Biotechnology	Cat#sc-398011; N/A
mouse anti-FoxP1	Abcam	Cat#ab32010; RRID: AB_1141518
rabbit anti-FoxP1	Abcam	Cat#ab16645; RRID: AB_732428
rat anti-Ctip2	Abcam	Cat#ab18465; RRID: AB_2064130
mouse anti-TH	Millipore	Cat#MAB318; RRID: AB_2201528
mouse anti-Sox2	Abcam	Cat#ab79351; RRID: AB_10710406
rabbit anti-Sox2	Millipore	Cat#ab5603; RRID: AB_2286686
sheep anti-Vsx2	Abcam	Cat#ab16141; RRID: AB_302278
rabbit anti-Nkx6-1	Novus Biologicals	Cat#NBP1-49672SS; RRID: AB_10011793
goat anti-CtB	List Biologicals	Cat#703; N/A
rabbit anti-Otp	a gift from Flora Vaccarino	N/A
mouse anti-Pax3	DSHB	Cat#AB_528426; RRID: AB_528426
rabbit anti-Pax5	Abcam	Cat#ab109443; RRID: AB_10862070
mouse anti-Pax7	DSHB	Cat#AB_528428; RRID: AB_528428
goat anti-Parvalbumin	Swant	Cat#PVG213; RRID: AB_2721207
mouse anti-Calbindin	Swant	Cat#CB300; N/A
rabbit anti-RFP	Rockland	Cat#600-401-379; RRID: AB_2209751
mouse anti-BrdU	GE Healthcare Life Sciences	Cat#RPN20AB; RRID: AB_2314032
mouse anti-HuC/D	Thermo Fisher Scientific	Cat# A-21271; RRID: AB_221448
rabbit anti-pHistone H3	Millipore	Cat# 06-570; RRID: AB_310177
Rabbit anti-Notch1 ICD	Cell Signaling Technology	Cat# 4147, RRID: AB_2153348
donkey anti-rabbit IgG Alexa Fluor 568	Thermo Fisher Scientific	Cat#A10042; RRID: AB_2534017
donkey anti-mouse IgG Alexa Fluor 488	Thermo Fisher Scientific	Cat#A-21202; RRID: AB_141607
donkey anti-rabbit IgG Alexa Fluor 488	Thermo Fisher Scientific	Cat#A-21206; RRID: AB_2535792
donkey anti-rabbit IgG Alexa Fluor 647	Thermo Fisher Scientific	Cat#A-31573; RRID: AB_2536183
donkey anti-mouse IgG Alexa Fluor 568	Thermo Fisher Scientific	Cat#A10037; RRID: AB_2534013
donkey anti-mouse IgG Alexa Fluor 647	Thermo Fisher Scientific	Cat#A-31571; RRID: AB_162542
donkey anti-sheep IgG Alexa Fluor 488	Abcam	Cat#ab150177; RRID: AB_2801320
donkey anti-sheep IgG Alexa Fluor 568	Thermo Fisher Scientific	Cat#A21099; RRID: AB_10055702
donkey anti-rat IgG Alexa Fluor 488	Thermo Fisher Scientific	Cat#A-21208; RRID: AB_2535794
donkey anti-rat IgG Alexa Fluor 568	Abcam	Cat#AB175475; RRID: AB_2636887
donkey anti-goat IgG Alexa Fluor 568	Thermo Fisher Scientific	Cat#A-11057; RRID: AB_2534104
donkey anti-goat IgG Alexa Fluor 647	Abcam	Cat#ab150135; RRID: AB_2687955
donkey anti-goat IgG Alexa Fluor 488	Thermo Fisher Scientific	Cat#A-11055; RRID: AB_2534102
Deposited Data		
Raw and processed scRNA-seq data	Gene Expression Omnibus	GEO: GSE157964
Raw and processed RNA-seq data	Gene Expression Omnibus	GEO: GSE157964
Gene expression visualization in the scRNaseq data	RStudio Shiny based service	http://tegex.helsinki.fi/
Experimental Models: Organisms/Strains		
En1Cre: STOCK *En1*$^{tm2(cre)Wrst}$/*J*	The Jackson Laboratory	Cat#JAX:007916; RRID:I MSR_JAX:007916
Sox14Gfp	Delogu et al., 2012	N/A

(*Continued on next page*)

Continued

REAGENT or RESOURCE	SOURCE	IDENTIFIER
Tal1flox	Bradley et al., 2006	N/A
Zfpm2flox: *Zfpm2*^{tm2Sho}/*EiJ*	Manuylov et al., 2007	Cat#JAX:007266; RRID: IMSR_JAX:007266
R26R^{TdTomato}: *B6.Cg-Gt(ROSA) 26Sor*$^{tm9(CAG-tdTomato)Hze}$/*J*	The Jackson Laboratory	Cat#JAX:007909; RRID: IMSR_JAX:007909
Pax7Cre: STOCK *Pax7*$^{tm1(cre)}$*Mrc/J*	The Jackson Laboratory	Cat#JAX:010530; RRID: IMSR_JAX:010530
Vglut2Cre: *Slc17a6*$^{tm2(cre)Lowl}$/*Slc17a6*$^{+}$	The Jackson Laboratory	Cat#5141283; RRID:MGI:5141283
Gad67^{EGFP}	Tamamaki et al., 2003	N/A
Psen1^{tm1Bdes}	De Strooper et al., 1998	INFRAFRONTIER: EM:00303
Oligonucleotides		
Primer for genotyping sex	McFarlane et al., 2013	N/A
SX_F: GAT GAT TTG AGT GGA AAT GTG AGG TA		
SX_R: CTT ATG TTT ATA GGC ATG CAC CAT GTA		
Software and Algorithms		
GraphPad Prism v.8	GraphPad Software	https://www.graphpad.com/scientific-software/prism/
SPSS Statistics v.25	IBM	https://www.ibm.com/analytics/spss-statistics-software
Adobe Photoshop CC 2018	Adobe	https://www.adobe.com/products/photoshop.html
Adobe Illustrator CC 2018	Adobe	https://www.adobe.com/products/illustrator.html
ImageJ v1.50i	NIH	https://imagej.nih.gov/ij/
Imaris	Bitplane Scientific Software	https://imaris.oxinst.com/packages
InDrop scripts	Klein et al., 2015; Zilionis et al., 2017	N/A
Trimmomatic	Bolger et al., 2014	http://www.usadellab.org/cms/?page=trimmomatic
Bowtie	Langmead et al., 2009	http://bowtie-bio.sourceforge.net/index.shtml
R	R Core Team	https://www.R-project.org
scater	McCarthy et al., 2017	https://bioconductor.org/packages/release/bioc/html/scater.html
scran	Lun et al., 2016	https://bioconductor.org/packages/release/bioc/html/scran.html
Seurat	https://satijalab.org/seurat	https://cran.r-project.org/web/packages/Seurat/index.html
Monocle 2	Qiu et al., 2017	http://bioconductor.org/packages/release/bioc/html/monocle.html
Monocle 3	Trapnell et al., 2014	https://cole-trapnell-lab.github.io/monocle3/
STAR	Dobin et al., 2013	https://github.com/alexdobin/STAR
featureCounts	Liao et al., 2014	https://bioconductor.org/packages/release/bioc/html/Rsubread.html
limma	Ritchie et al., 2015	http://bioconductor.org/packages/release/bioc/html/limma.html
sva	Leek et al., 2012	http://bioconductor.org/packages/release/bioc/html/sva.html
umap	Becht et al., 2018	https://github.com/lmcinnes/umap
ClusterMap	Gao et al., 2019	https://github.com/xgaoo/ClusterMap

(*Continued on next page*)

Continued

REAGENT or RESOURCE	SOURCE	IDENTIFIER
Other		
In situ probe: mouse Dll1	RZBD	IRAVp968B07112D6
In situ probe: mouse En1	Davis and Joyner, 1988	N/A
In situ probe: mouse Foxo1	Allen brain Atlas	RP_050407_02_B11
In situ probe: mouse Gad1	Guimera et al., 2006	N/A
In situ probe: mouse Gata3	Lilleväli et al., 2004	N/A
In situ probe: mouse Lhx4	Source BioScience	IMAGE4507576
In situ probe: mouse Lhx9	Source BioScience	IRAVp968E08130D
In situ probe: mouse Lmx1a	Source BioScience	IMAGE317647
In situ probe: mouse Lmx1b	a gift from Horst Simon	N/A
In situ probe: mouse Pdzk1ip1	This paper	NCI_CGAP_Kid14
In situ probe: mouse Mnfg	This paper	NCI_CGAP_Mam
In situ probe: mouse Netrin	Serafini et al., 1994	N/A
In situ probe: mouse NeuroD6	Kay et al., 2011	N/A
In situ probe: rat Nr4a2	a gift Thomas Perlmann	N/A
In situ probe: mouse Otx1	Simeone et al., 1993	N/A
In situ probe: mouse Pdzrn4	Source BioScience	RIKEN ID6820442M07
In situ probe: mouse Pnoc	Source BioScience	IMAGE ID8734121
In situ probe: mouse Prph	This paper	NCI_CGAP_Co24
In situ probe: mouse Sall3	Allen brain Atlas	RP_051121_01_B02
In situ probe: mouse Sert	Allen brain Atlas	RP_071204_04_G10
In situ probe: mouse Six3	Source BioScience	IMAGp998B1912702Q
In situ probe: mouse Skor1	Allen Brain Atlas	RP_100908_02_A06
In situ probe: mouse Sox14	Source BioScience	IMAGp998A2414391Q
In situ probe: mouse Sst	Source BioScience	IMAGp998H231140Q
In situ probe: mouse St18	Kameyama et al., 2011	N/A
In situ probe: mouse Cnctn2	Denaxa et al., 2001	N/A
In situ probe: mouse Tal1	Source BioScience	IRAVp968D09118D
In situ probe: mouse Tlx3	Cheng et al.,2004	N/A
In situ probe: mouse Vglut2	Guimera et al., 2006	N/A
In situ probe: mouse Vsx2	a gift from Robert Chow	N/A
In situ probe: mouse Zic1	Allen Brain Atlas	RP_051017_03_A02
In situ probe: mouse Zfpm1	Source BioScience	IMAGE ID3585094
In situ probe: mouse Zfpm2	Source BioScience	IRAVp968B06115D

RESOURCE AVAILABILITY

Lead Contact

Further information and requests for resources and reagents should be directed to and will be fulfilled by the Lead Contact, Juha Partanen (juha.m.partanen@helsinki.fi).

Materials Availability

This study did not generate new unique reagents.

Data and Code availability

The accession number of the bulk and single-cell mRNA sequencing data reported in this paper is GEO: GSE157964).

The gene expression across the E12.5 and E13.5 wild-type mouse r1 cell clusters can be viewed at URL http://tegex.helsinki.fi/

EXPERIMENTAL MODEL AND SUBJECT DETAILS

Animals

The following mouse lines were used in the study: *En1*^{Cre} (Kimmel et al., 2000), *Sox14*^{Gfp} (Delogu et al., 2012), *Fog2*^{flox} (Manuylov et al., 2007), *Tal1*^{flox} (Bradley et al., 2006), *R26R*^{TdTomato} (Madisen et al., 2010), *Pax7*^{Cre} (Keller et al., 2004), *Vglut2*^{Cre} (Vong et al., 2011), *Gad67*^{EGFP} (Tamamaki et al., 2003), *Psen1*^{null} (De Strooper et al., 1998). Mice were maintained on ICR background except *Sox14*^{Gfp} (C57BL/6), *Pax7*^{Cre} (C57BL/6J), *Vglut2*^{Cre} (C57BL/6J). E12.5, E13.5, E14.5, E15.5, E18.5, P0.5 and adult (2-3 month old) mice were used in this study. Except for the single-cell mRNAsequencing experiments, the sex of the embryonic mice was not determined. Females were used for analysis of the adults. Littermates were used as a controls. All the experiments with these mice were approved by the Laboratory Animal Center, University of Helsinki, and the National Animal Experiment Board in Finland.

METHOD DETAILS

Histology

For the IHC and *in situ* hybridization studies, E12.5-E15.5 embryos or E18.5-P0.5 brains were dissected, fixed in the 4% paraformaldehyde (PFA; Sigma-Aldrich, Cat#P6148) in 1xPBS for two days. For the adult brains, the mice were perfused intracardially with 4% PFA, brains were dissected, and fixed for two days. The fixed brains were embedded in the paraffin and 5-10μm thick sections were made with Leica RM2255.

Immunohistochemistry

The paraffin sections were rehydrated, permeabilized for 10 min with 0.3% Triton X-100 (Sigma-Aldrich, Cat#T9284) in PBS and antigens were retrieved by boiling the sections in 0.1M Na-citrate buffer (pH 6) in the microwave oven for 15 min. The sections were blocked with 10% donkey serum (Biowest, Cat#S2170) in 0.1% Triton X-100 solution for 1 h after what slides were incubated with primary antibody (diluted in the blocking solution) over night at +4°C. On the next day, the sections were incubated with secondary antibodies for 4 h at room temperature and counter-stained with DAPI (4',6-diamidino-2-phenylindole; Sigma-Aldrich, Cat#D9564) to visualize the nuclei. Dilutions of primary antibodies used in this study: rabbit anti-Foxo1 (1:500, Cat#2880; RRID: AB_2106495), rabbit anti-Zfpm2 (1:200, Cat#sc-10755; RRID: AB_2218978), mouse anti-Zfpm2 (1:200, Santa Cruz Biotechnology; Cat#sc-398011), mouse anti-FoxP1 (1:500, Cat#ab32010; RRID: AB_1141518), rabbit anti-FoxP1 (1:400, Cat#ab16645; RRID: AB_732428), rat anti-Ctip2 (1:500, Cat#ab18465; RRID: AB_2064130), mouse anti-TH (1:600, Cat#MAB318; RRID: AB_2201528), mouse anti-Sox2 (1:800, Cat#ab79351; RRID: AB_10710406), rabbit anti-Sox2 (1:400, Cat#ab5603; RRID: AB_2286686), sheep anti-Vsx2 (1:500, Cat#ab16141; RRID: AB_302278), rabbit anti-Nkx6-1 (1:400, Cat#NBP1-49672SS; RRID: AB_10011793), goat anti-CtB (1:10000, List Biologicals; Cat#703), rabbit anti-Otp (1:2000, kindly provided by Flora Vaccarino), mouse anti-Pax3 (1:300, Cat#AB_528426; RRID: AB_528426), rabbit anti-Pax5 (1:500, Cat#ab109443; RRID: AB_10862070), mouse anti-Pax7 (1:300, Cat#AB_528428; RRID: AB_528428), goat anti-Pvalb (1:2000, Cat#PVG213; RRID: AB_2721207), mouse anti-Calb1 (1:2500, Swant; Cat#CB300), rabbit anti-RFP (1:500, Cat#600-401-379; RRID: AB_2209751), mouse anti-BrdU (1:600, Cat#RPN20AB; RRID: AB_2314032), mouse anti-HuC/D (1:200, Cat# A-21271; RRID: AB_221448), rabbit anti-pHistone H3 (1:800, Cat# 06-570; RRID: AB_310177), rabbit anti-Notch1-ICD (1:400, Cat# 4147, RRID: AB_2153348). Secondary antibodies used in this study (1:400): donkey anti-rabbit IgG Alexa Fluor 568 (Cat#A10042; RRID: AB_2534017), donkey anti-mouse IgG Alexa Fluor 488 (Cat#A-21202; RRID: AB_141607), donkey anti-rabbit IgG Alexa Fluor 488 (Cat#A-21206; RRID: AB_2535792), donkey anti-rabbit IgG Alexa Fluor 647 (Cat#A-31573; RRID: AB_2536183), donkey anti-mouse IgG Alexa Fluor 568 (Cat#A10037; RRID: AB_2534013), donkey anti-mouse IgG Alexa Fluor 647 (Cat#A-31571; RRID: AB_162542), donkey anti-sheep IgG Alexa Fluor 488 (Abcam, Cat#ab150177), donkey anti-sheep IgG Alexa Fluor 568 (Cat#A21099; RRID: AB_10055702), donkey anti-rat IgG Alexa Fluor 488 (Cat#A-21208; RRID: AB_2535794), donkey anti-rat IgG Alexa Fluor 568 (Cat#AB175475; RRID: AB_2636887), donkey anti-goat IgG Alexa Fluor 647 (Cat#ab150135; RRID: AB_2687955), donkey anti-goat IgG Alexa Fluor 488 (Cat#A-11055; RRID: AB_2534102).

mRNA *in situ* hybridization

mRNA *in situ* hybridization (ISH) was carried out using digoxigenin- or fluorescein-labeled cRNA probes that were synthesized with specific RNA labeling kits (Roche, Cat#11277073910 and Cat#11685619910 respectively) as recommended by the manufacturer.

The following cRNA *in situ* probes were used in this study: *Dll1* (RZBD, IRAVp968B07112D6), *En1* (Davis and Joyner, 1988), *Foxo1* (RP_050407_02_B11 from Allen Brain Atlas, (Lein et al., 2007)), *Gad1* (Guimera et al., 2006), *Gata3* (Lilleväli et al., 2004), *Lhx4* (Source BioScience, IMAGE4507576), *Lhx9* (Source BioScience, IRAVp968E08130D), *Lmx1a* (Source BioScience, IMAGE317647), *Lhx1b* (a gift from Horst Simon), *Pdzk1ip1* (NCI_CGAP_Kid14), *Mnfg* (NCI_CGAP_Mam), *Netrin* (Serafini et al., 1994), *NeuroD6* (Kay et al., 2011), *Norr1* (a gift Thomas Perlmann), *Otx1* (Simeone et al., 1993), *Pdznrn4* (Source BioScience, RIKEN ID6820442M07), *Pnoc* (Source BioScience, IMAGE ID8734121), *Prph* (NCI_CGAP_Co24), Sall3 (RP_051121_01_B02 from Allen Brain Atlas, (Lein et al., 2007)), *Sert* (RP_071204_04_G10 from Allen Brain Atlas (Lein et al., 2007)), *Six3* (Source BioScience, IMAGp998B1912702Q), Skor1 (RP_100908_02_A06 from Allen Brain Atlas, (Lein et al., 2007)), *Sox14* (Source BioScience, IMAGp998A2414391Q), *Sst* (Source BioScience, IMAGp998H231140Q), *St18* (Kameyama et al., 2011), *Cnctn2* (Denaxa et al., 2001), *Tal1* (Source BioScience, IRAVp968D09118D), *Tlx3* (Cheng et al., 2005), *Vglut2* (Guimera et al., 2006), *Vsx2* (a gift from Robert Chow), *Zic1*

(RP_051017_03_A02 from Allen Brain Atlas (Lein et al., 2007)), *Zfpm1* (Source BioScience, IMAGE ID3585094), *Zfpm2* (Source BioScience, IRAVp968B06115D).

Paraffin sections were rehydrated using xylene-ethanol series, permeabilized for 10 min with 0.3% Trition X-100 in PBS. Antigens were retrieved by boiling the sections in 0.1M Na-citrate buffer (pH 6) in the microwave oven for 15 min. Sections were permeabilized using 20% SDS (Sodium dodecyl sulfate) in PBS for 15 min and treated with 0.25% acetic anhydride (Sigma-Aldrich, Cat#33214) in 0.1M TEA (Triethanolamine; Sigma-Aldrich, Cat#33729) for 10 min on a shaker. Sections were hydrated using graded ethanol series and dried. Probes were diluted (1:400) in the hybridization buffer (10% Dextran sulfate (Sigma-Aldrich, Cat#D8906), 0.3M NaCl, 20mM Tris-HCl (pH 8.0), 5mM EDTA (pH 8.0), 1xDenhardt's solution (Sigma-Aldrich, Cat#D2532), 50% Ultrapure formamide (Invitrogen, Cat#15515-026), 500ug/ml Yeast RNA (Sigma, Cat#R6750)) and added to the slides. Slides were incubated over night at +65°C. The slides were washed with 5xSSC, followed by a wash in 50% formamide (Millipore, Cat#75-12-7) in 2xSSC in water bath at +65°C for 1 h. Slides were treated with RNase A (0,02mg/ml, Roche, Cat#10109169001) in NTE (0.5M NaCl, 5mM Tris-HCl pH8.0, 5mM EDTA pH8.0) at +37°C for 1 h. Slides were blocked with TNB blocking buffer (0.1M Tris-HCl pH7.5, 0.15M NaCl, 0.5% blocking reagent (Perkin Elmer, Cat#FP1012)) for 1 h and incubated with sheep anti-Digoxigenin-POD Fab fragments antibody (Roche, Cat#11207733910, 1:800) or sheep anti-Fluorescein-POD, Fab fragments (Roche, Cat#11426346910, 1:800) antibody at +4°C overnight. The TSA Plus Cyanine 3.5 (PerkinElmer, Cat#NEL763B001KT) or Fluorescein system (PerkinElmer, Cat#NEL741B001KT) was used to detect the antibody.

To combine ISH with IHC, the normal IHC was carried out on the slides starting with the blocking step. For double ISH, two different probes (digoxigenin and fluorescein labeled) were incubated simultaneously. The fluorescein-labeled probe was detected with the TSA Plus Fluorescein system. After the TSA Plus Fluorescein detection, peroxidase activity was quenched with 0.2N HCl for 40 min, and slides were incubated with sheep anti-Digoxigenin-POD Fab fragments antibody at +4°C overnight and visualized with TSA Plus Cyanine 3.5 kit.

EdU and BrdU labeling

For the birth-dating analysis, pregnant ICR females were injected with EdU (1mg/kg, Molecular Probes, Cat#C10338) or BrdU (2mg/kg, Sigma, Cat#B5002) at noon of E10.5, E11.5, E12.5 or E13.5. Embryos where collected at P0.5, fixed and paraffin sections were made like described in the histology. To visualize the EdU or BrdU positive nuclei, normal IHC was carried out. For EdU, Click-iT EdU Alexa Fluor 555 Imaging Kit (Molecular Probes, Cat#C10638) was used before the blocking step, while BrdU was detected using a mouse anti-BrdU antibody (GE Healthcare Life Sciences, Cat#RPN20AB).

Stereotaxic surgery and neuronal labeling

For retrograde tracing, eight week old wild-type ICR mice were used. Mice were anesthetized with isoflurane and attached to the stereotaxic frame. Small hole was drilled into the skull and unilateral, intracranial injections of 300nl of 0.2% Choleratoxin B subunit (CtB; List Biological Lab.Inc. Cat#104) was injected at the speed of 50nl/min using a microinjector (UltraMicroPump III, World Precision Instruments) and microsyringe (Hamilton, Cat#7803-06). Stereotaxic coordinates were measured from bregma in mm. To trace the LDTg neurons, CtB was injected into VTA: −3.1 (AP); 0.36 (ML); −4.65 (DV). Four to six days after the injections mice were intracardially perfused with 4% PFA and brains were collected, thereafter brains were fixed in 4% PFA for 24 h. 100 μm vibratome sections were cut for IHC stainings. Sections were blocked for 1 h in 10% donkey serum in PBS containing 05% Triton X-100 (PBS-T), followed by incubation overnight at room temperature with following antibodies diluted in PBS-T: rabbit anti-Nkx6-1 (1:400, Novus Biologicals); goat anti-CtB (1:5000, List Biologicals #703); mouse anti-TH (1:1000, Merck Millipore) and DAPI. Secondary antibodies conjugated to Alexa 488, 594, or 647 were used for detection. ProLong Gold anti-fade mounting media was used for mounting (Thermo Fisher Scientific, P36930).

Imaging

Images were taken with Olympus BX63 microscope with the DP72 camera or TCS SP5 (Leica) laser scanning microscope with Plan Apochromat 20x/0.7 NA glycerol objective. Images were processed with Imaris (Bitplane Scientific Software) and Adobe Photoshop CC 2018 and Adobe Illustrator CC 2018 software.

RNA sequencing

RNA extraction

Tissue from the E12.5 ventral r1 of 6 *Ctrl* and 6 *Tal1*^{cko} embryos were dissected in DMEM. The tissue was frozen in liquid nitrogen and stored at −80°C. The samples were homogenized in Precellys CK14 tubes with the Precellys 24 homogenizer (Bertin Technologies) for 30 s at 5000 rpm. Total RNA was isolated with Trizol Reagent/chloroform extraction using Direct-zol RNA MiniPrep columns (Zymo research, catalog # R2051) followed by DNase I digestion, according to manufacturer's instructions. The RNA concentrations was measured spectrophotometrically using NanoDrop2000 (Thermo Scientific). RNA quality was assayed on RNA Nano Chips (Agilent) with Agilent Bioanalyzer 2100 according to manufacturer's instructions. All samples used for RNA-seq had RNA integrity number (RIN) value of at least 9.4.

Sequencing and quality control of data

Sequencing libraries were prepared using the TruSeq Stranded Total RNA Sample Preparation Kit (Illumina) with Ribo-Zero rRNA depletion. The libraries were sequenced in one run with the Illumina NextSeq500 sequencer producing 400 million single reads of 86 base pairs. The average sequencing depth per sample was ~33 million reads.

Read mapping and expression quantification

The reference genome build used for mapping was UCSC mm10, downloaded from Illumina's iGenomes collection on 07.06.2015 at https://support.illumina.com/sequencing/sequencing_software/igenome.html. The adaptor-trimmed sequencing reads were mapped to the reference genome with STAR 2.4 (Dobin et al., 2013). The suffix array used by STAR for mapping was generated using mm10 RefSeq gene annotation as a splice junction database. The annotation was downloaded in Gene Transfer Format (GTF) from the UCSC Table Browser at http://genome-euro.ucsc.edu/ (accessed on 08.06.2015). Gene-level read counts from uniquely mapped reads overlapping exons were obtained with the featureCounts function from the R package Rsubread version 1.16.1 (Liao et al., 2014). The RefSeq gene annotation for genome build mm10 provided by Rsubread was used for expression quantification after removing mitochondrial and rRNA annotations. The option for strand-specific read counting was used.

Differential expression analysis

The analysis of differential expression was carried out with the R package limma 3.24.12 (Ritchie et al., 2015). Lowly expressed and uninformative genes, based on counts per million (cpm) values, were removed as recommended (Anders et al., 2013). Genes with cpm over one in all samples and over five in at least six samples were kept. The counts were transformed with the function voomWithQualityWeights using TMM-normalized library sizes. The expression values were adjusted for effects due to RNA extraction and dissection dates with the function ComBat of the R package sva version 3.14.0 (Leek et al., 2012). A linear model with the genotype group as a predictor variable was fit to the adjusted data with the limma function lmFit. Empirical Bayes statistics were calculated for the linear model fit using the limma function eBayes and used to rank genes in order of evidence for differential expression. The false discovery rate (FDR) was controlled for by using the Benjamini-Hochberg procedure (Benjamini and Hochberg, 1995). An adjusted p value of 0.05 was used as the threshold of significance.

Validation of selected differentially expressed genes by RT-qPCR

For validation, the expression of ten genes with different fold changes ($|\log2FC| \geq 0.5$; *Asic4, Cbfa2t3, Hs6st1, Id4, Lhx4, Otx1, Pdzk1ip1, Shox2, Skor1 and Sst*) was analyzed by RT-qPCR in 3 *Ctrl* and 3 $Tal1^{cko}$ E12.5 r1 samples not used for sequencing. One negative (*Pax7*) and four positive controls (*Gad1, Gata3, Tal1, Vsx2*) with known expression patterns were included in the analysis. The reactions were run using Power SYBR Green (Applied Biosystems, catalog #4367659) and thermal cyclers Bio-Rad C1000 and Bio-Rad C1000 Touch. The efficiencies and R^2 values were calculated with Bio-Rad CFX Manager software version 3.1.1517.0823. All analyzed genes showed expression changes to the expected direction. All positive controls and seven candidate genes (*Asic4, Cbfa2t3, Id4, Otx1, Pdzk1ip1, Shox2* and *Sst*) were differentially expressed with an FDR of 10%. Genes *Gad1, Gata3, Id4, Otx1, Pdzk1ip1* and *Sst* were differentially expressed with an FDR of 5%. The corresponding fold change estimates from RNA-seq and RT-qPCR were generally close to each other, with a Pearson's correlation coefficient of 0.93 (data not shown).

Single-cell mRNA sequencing

Dissection of ventral r1 and cell dissociation

Ventral r1 of E12.5 and E13.5 embryos (Table S1) was dissected in the 5% FBS (fetal bovine serum; Millipore, Cat#ES-009-B) in L-15 (GIBCO, Cat#11415-049) medium on ice. Vascular and mesenchymal tissues surrounding the midbrain and hindbrain were removed. The r1 was separated from the midbrain using a visible constriction at the midbrain-hindbrain boundary as a landmark. The border between r1 and r2 was estimated using $En1^{Cre}$; $R26R^{TdTomato}$ embryos as a reference. The ventral part of the r1 (area indicated in Figure 1B) was separated and transferred into a new Petri dish with dissection medium. The tissue was cut into smaller pieces with a knife and the pieces were collected into an Eppendorf tube. The pieces were washed 3 times with 500 μl of cold PBS (Lonza, Cat#BE17-516Q) by centrifuging them at 100 g (+4°C) for 5 min. R1 tissue was dissociated using the Papain Dissociation System (Worthington, Cat#LK003150) for 1 h at 37°C and processed as previously described (Chakrabarty et al., 2012). Cells were washed 3 times in cold PBS, counted, and their viability was determined before encapsulation. The genotype and the sex of the embryos was determined by PCR (sex-specific primers: SX_F: 5′GATGATTTGAGTGGAAATGTGAGGTA'3 and SX_R: 5′CTTATGTTTATA GGCATGCACCATGTA'3 (McFarlane et al., 2013)). Samples containing at least 92% of viable cells were used for barcoding.

The sample information and sequencing statistics are shown in Table S1.

Barcoding and library preparation

Chromium Single Cell 3′RNaseq platform (10x Genomics) and InDrop technology (Klein et al., 2015; Zilionis et al., 2017) were used for single-cell mRNA sequencing library preparation. The Chromium Single Cell 3′RNaseq run and library preparation were done using the Chromium Single Cell 3′ Reagent version 3 chemistry. Briefly, in both platforms, the dissociated single cells are co-encapsulated into 3-4nl droplets together with barcoded hydrogel beads and a mixture of reverse-transcription (RT) and lysis reagents. Within every single droplet, a cell is lysed and cDNA tagged with a barcode during reverse transcription. The droplet emulsion is then broken and the bulk material taken through the following steps: i) second strand synthesis; ii) linear amplification by *in vitro* transcription (IVT);

amplified RNA fragmentation; iv) reverse transcription; v) PCR. The InDrop cDNA libraries were multiplexed and sequenced on NextSeq Illumina platform in paired-end mode using high-yield 75 cycle kit). The Chromium 10xGenomics cDNA libraries were sequenced on Illumina NovaSeq 6000 system using read lengths: 28bp (Read 1), 8bp (i7 Index), 0 bp (i5 Index) and 89bp (Read 2). Read quality was assessed by running FASTQC (version 0.10.1).

Processing of the single-cell mRNA sequencing reads

InDrop data processing

Previously published Python scripts were used to process the sequencing reads and to generate count matrices (Klein et al., 2015; Zilionis et al., 2017) (GEO:GSE157964). Briefly, raw transcript reads were trimmed with Trimmomatic 0.36 (Bolger et al., 2014), and barcode reads were filtered for expected structure (known cellular barcode, W1 sequence, poly-T tail). Filtered reads were sorted based on barcodes, and barcodes having at least 12 000 reads were kept (568 control barcodes and 1099 Tal1^{cko} barcodes). The filtered reads were aligned with bowtie 1.1.1 (Langmead et al., 2009) to the Ensembl GRCm38 cDNA reference. A poly-A sequence of 125 bases was added to each transcript before building the bowtie index. For UMI quantification, a minimum of 10 bases were required to overlap non-poly-A sequence in the aligned transcript reads. Only unambiguous UMI counts were kept. Modifications to the original scripts include a hamming distance of 5 for W1 sequence matching and minimum poly-T length of 3 for the barcode reads. Percentages of unaligned reads per barcode were recorded from the script output and used in count matrix quality control. For quality control, we used the R package scater 1.4.0 (McCarthy et al., 2017) with the following criteria: we removed all cells with a, over 50% unmapped reads, b, with total numbers of counts and detected genes 3 median-absolute-deviations above or below the median (log10 scale), or c, with over 2% apoptosis gene counts or over 5% mitochondrial counts. Genes annotated with the GO term "positive regulation of apoptotic process" (GO:0043065; evidence codes EXP, IDA, IEP, IGI, IMP, IPI) were used for filtering apoptotic outliers. Genes with average counts below 0.03 were filtered out. Gene expression counts were normalized with size factors computed with the R package scran 1.4.5 (Lun et al., 2016). After quality control, 458 control cells and 900 Tal1cko cells remained (Table S1). To avoid removing biological differences between the samples, no batch adjustment was performed for the two E12.5 samples (which were processed on different days) due to the confounding of processing date and genotype.

Chromium 10xGenomics data processing

Genome alignment and gene expression scoring were performed using recommended 10x Genomics Cell Ranger v3.0.1 pipelines. The reference genome was mouse mm10. The quality filtered count matrix included 15027 E12.5 cells and 15719 E13.5 cells. Before the downstream analyses, we filtered the count matrix, removing cells where either a, less than 300 features, b, over 7000 features, or c, over 15% of mitochondrial associated genes were detected. The filtered count data were normalized within the Seurat package using the normalization.method "LogNormalize," and scale.factor = 1e4.

Clustering analyses of the single-cell mRNA sequencing data

InDrop clustering

Clustering was performed with the R package Seurat 1.4.0 (Rahul Satija (NA). Seurat: R toolkit for single cell genomics. R package version 1.4.0. https://satijalab.org/seurat). Highly variable genes (HVGs) were identified with the Seurat function MeanVarPlot using the following arguments: y.cutoff = 1.5, x.low.cutoff = 0, x.high.cutoff = 3. The total number of counts (nUMI) was regressed out with a negative binomial generalized linear model, and the data were centered and scaled. Dimensionality of the data were reduced with PCA calculated using the HVGs.

The cells were clustered with the Seurat function FindClusters using the SLM modularity optimization algorithm (Blondel et al., 2008). For combined clustering of the control and Tal1cko samples, the following arguments were used: pc.use = 1:15, resolution = 2.3, k.param = 18, k.scale = 15.

DE genes for all pairs of clusters were identified with Seurat's function FindMarkers with the following arguments: min.pct = 0, test.use = "negbinom," thresh.use = log(1.5), only.pos = F, latent.vars = c("nUMI"). Cluster markers were identified with the Seurat function FindAllMarkers with the following arguments: thresh.use = log(1.5), test.use = "negbinom," min.pct = 0, only.pos = T, return.thresh = 1. p values for between-cluster DE genes and cluster markers were adjusted for multiple testing with the Benjamini-Hochberg procedure (Benjamini and Hochberg, 1995). An adjusted p value of 0.05 was set as the threshold of significance. For visualization of clusters, dimensionality reduction with t-SNE was performed using Seurat's RunTSNE function with the Barnes-Hut implementation and a perplexity of 30 (van der Maaten and Hinton, 2008).

Chromium 10xGenomics clustering

The data from E12.5 or E13.5 samples were clustered separately. Data from the samples of each stage were merged from filtered feature counts matrices (Cell Ranger). Graph-based clustering was performed with the R package Seurat 3.1.0., with default parameters unless mentioned below. We considered top 2000 highly variable genes in the clustering. Before clustering, genes were scaled and centered using the function ScaleData. To reduce the dimensionality of the data, we used PCA calculated using the top 2000 variable genes, and chose PCs 1-18 for the construction of the Shared Nearest Neighbor (SNN) Graph. The following parameters were used for clustering: dims = 1:18, resolution = 2.3 for E13.5 data and 2.5 for E12.5 data.

Clusters were visualized on a uniform manifold approximation and projection (UMAP) tools in Seurat (RunUMAP with argument dims = 1:18). Cluster specific genes (cluster markers) were identified with function FindAllMarkers and arguments only.pos = F, min.pct = 0.1, logfc.threshold = 0.25, test.use = "wilcox." Cell cycle phases were scored with function CellCycleScoring using Seurat's list of cell cycle associated genes (cc.genes).

Comparison of the E12.5 and E13.5 cell clusters

We used the R package ClusterMap 0.1.0 (Gao et al., 2019) to compare the cluster identities between the datasets from E12.5 and E13.5. To compare the datasets in an unbiased manner, the marker lists for both datasets were prepared using Seurat 3.1.0 function FindAllMarkers with arguments only.pos = T, min.pct = 0.1, logfc.threshold = 0.25, test.use = "wilcox"

As the number of cluster specific markers varies greatly, we standardized the marker lists by ordering the genes by average log fold change, and trimming the lists to the length of the maximum common length of the specific markers (28 markers in our case). Considering these 28 top markers for each cluster, the clusters were matched using the function cluster_map with edge_cutoff = 0.1.

To assess the statistical significance of the resulting cluster matches, we calculated the hypergeometric p value for each of the E12.5 – E13.5 cluster pairs. We collected all the unique marker genes, found in E12.5 and E13.5 and used the size of smaller of two sets as the size of background population. This generates slightly weaker correlations between the clusters, emphasizing real correlations.

Generated cluster pair correlation table stores $-\log_{10}$(p value) for each pair. When we visualized this data, strong outlier values dominated this visualization. Therefore, we used another *shifted log* function to lessen the effect of outliers in the visualization. The values shown represent $\log(-\log_{10}(\text{p value}) + 1)$ values.

Developmental trajectory (pseudotime) analyses

Analysis of rV2 GABAergic trajectory

Cells from E12.5 clusters 45,25,40,4,19,6,7 were ordered in pseudotime with the R package Monocle 2.12.0 (Qiu et al., 2017). A negative binomial distribution model was used for the gene expression data. Genes for ordering were selected by an unsupervised dpFeature procedure. The cells were reclustered and the top 1000 most significant differentially expressed genes were selected as the ordering genes. Dimensionality of the data were reduced with the DDRTree algorithm using relative expression values normalized with a variance-stabilizing transformation. Pseudotime-dependent genes were identified with the Monocle function differentialGeneTest using default arguments. A q-value of 0.001 was used as the threshold of statistical significance for pseudotime-dependent genes.

Analysis of branching of rV2 glutamatergic and GABAergic lineages

Cells from E13.5 rV2 GABAergic and glutamatergic precursors clusters 4, 5, 9, 12, 18, 28 and 36 were used for developmental lineage reconstruction. The pseudotime analysis was performed by R package monocle3, version 0.1.2. The developmental trajectory graph was calculated using monocle3 functions preprocess_cds (num_dim = 100), reduce_dimension, cluster_cells and learn_graph (use_partition = F). Cells were assigned a pseudotime value using the monocle3 function order_cells. The root of the pseudotime trajectory was chosen manually as the beginning of cluster 36 (precursors exiting the cell cycle). Based on the diverging expression of GABA- and glutamatergic marker genes, the first branchpoint (branchpoint 25) of the pseudotime trajectory was manually picked for further analysis using function choose_cells. Differentially expressed genes along the trajectory were identified with Moran's I test using function graph_test and resulting genes were filterd with q-value threshold q_value < 0.05, and grouped into co-expression modules with function find_gene_modules.

QUANTIFICATION AND STATISTICAL ANALYSIS

To quantify the cell numbers, cell counting was performed on at least 6 sections along the rostro-caudal r1 (for E12.5) or 12 sections (for E18.5), n = 3 for each genotype, using ImageJ (1.50i) or Adobe Photoshop CC 2018 (Adobe). Statistical analysis was done using SPSS Statistics (v.25; IBM) or GraphPad Prism (v.8; GraphPad Software). All the statistical parameters are described in the figure legends. To analyze the difference between two groups, we used the independent samples t test (Student's t test). Additionally, the data were analyzed for outliers (via boxplots), normality (normal distribution via Shapiro-Wilk test) and homogeneity of variances (via Levene's test). If one of these criteria was not met, the non-parametric Mann-Whitney U-test was carried out instead. When more than two groups were compared, we used two-way ANOVA with Bonferroni's multiple comparisons test. Data were represented as mean ± SEM. Fisher's exact test was used to evaluate the sample proportions in cell clusters. p values were adjusted for multiple testing using the Bonferroni procedure.